

AD-A043 127

PRATT AND WHITNEY AIRCRAFT GROUP WEST PALM BEACH FLA --ETC F/G 21/5  
ANALYTICAL AND EXPERIMENTAL STUDY OF SUBSONIC STALLED FLUTTER. (U)  
JUL 77 R A ARNOLDI, F O CARTA, R NI

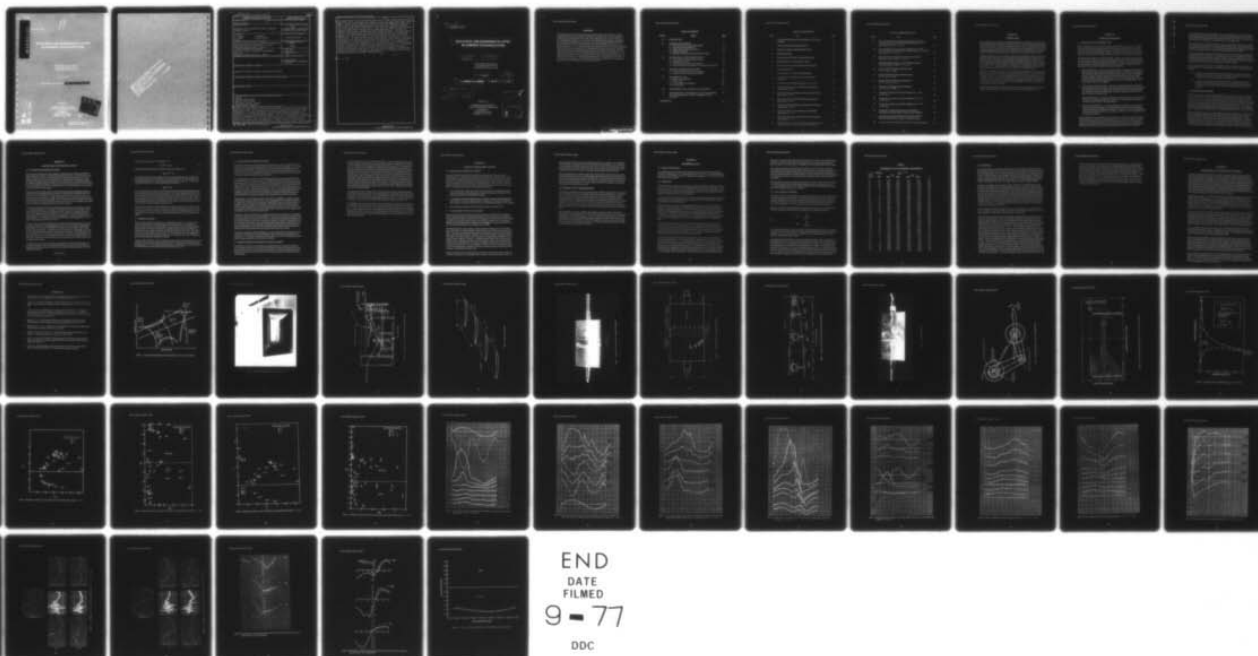
F44620-75-C-0066

UNCLASSIFIED

AFOSR-TR-77-0854

NL

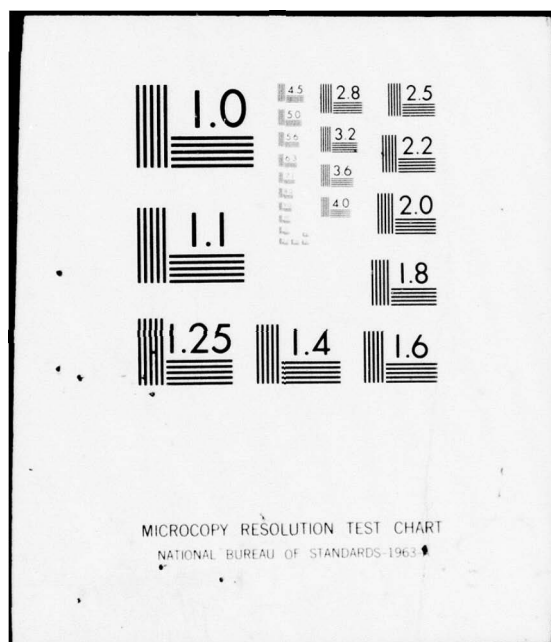
1 OF 1  
AD  
A043127



END  
DATE  
FILMED

9 - 77

DDC



AD A 043127

AFOSR-TR-77-0854

## ANALYTICAL AND EXPERIMENTAL STUDY OF SUBSONIC STALLED FLUTTER

Pratt & Whitney Aircraft Group  
Government Products Division  
West Palm Beach, Florida 44402

31 July 1977

Final Scientific Report for Period 1 April 1975 -- 31 May 1977

AD No. \_\_\_\_\_  
DDC FILE COPY

Prepared for  
UNITED STATES AIR FORCE  
OFFICE OF SCIENTIFIC RESEARCH  
Building 410  
Bolling Air Force Base  
Washington, D. C. 20332



Approved for public release;  
distribution unlimited.

AIR FORCE OFFICE OF SCIENTIFIC RESEARCH (AFOSR)  
OFFICE OF TRANSMITTAL TO DDC  
This technical report has been reviewed and is  
approved for public release IAW AFR 190-15 (7b).  
Distribution is unlimited.  
A. D. ELSON  
Technical Information Officer



UNCLASSIFIED

SECURITY CLASSIFICATION OF THIS PAGE (When Data Entered)

REPORT DOCUMENTATION PAGE		READ INSTRUCTIONS BEFORE COMPLETING FORM
1. REPORT NUMBER AFOSR TR-77-0854	2. GOVT ACCESSION NO.	3. RECIPIENT'S CATALOG NUMBER
4. TITLE (and Subtitle)  ANALYTICAL AND EXPERIMENTAL STUDY OF SUBSONIC STALLED FLUTTER		5. TYPE OF REPORT & PERIOD COVERED FINAL 1 April 1975 - 31 May 1977
		6. PERFORMING ORG. REPORT NUMBER
7. AUTHOR(s) R A ARNOLDI                      W N DALTON F O CARTA                        A O ST HILAIRE R-H NI		8. CONTRACT OR GRANT NUMBER(s)  F44620-75-C-0066
9. PERFORMING ORGANIZATION NAME AND ADDRESS PRATT & WHITNEY AIRCRAFT GROUP/United Technologies GOVERNMENT PRODUCTS DIVISION/PO BOX 2691 WEST PALM BEACH, FLORIDA 33402		10. PROGRAM ELEMENT, PROJECT, TASK AREA & WORK UNIT NUMBERS 2307A4  61102F
11. CONTROLLING OFFICE NAME AND ADDRESS AIR FORCE OFFICE OF SCIENTIFIC RESEARCH/NA BLDG 410 BOLLING AIR FORCE BASE, D C 20332		12. REPORT DATE July 1977
		13. NUMBER OF PAGES 57
14. MONITORING AGENCY NAME & ADDRESS (if different from Controlling Office)		15. SECURITY CLASS. (of this report)  UNCLASSIFIED
		15a. DECLASSIFICATION/DOWNGRADING SCHEDULE
16. DISTRIBUTION STATEMENT (of this Report)  Approved for public release; distribution unlimited.		
17. DISTRIBUTION STATEMENT (of the abstract entered in Block 20, if different from Report)		
18. SUPPLEMENTARY NOTES		
19. KEY WORDS (Continue on reverse side if necessary and identify by block number) FLUTTER UNSTEADY AERODYNAMICS SUBSONIC STALL FLUTTER OSCILLATING AIRFOIL CASCADES TURBOMACHINERY VIBRATION		
20. ABSTRACT (Continue on reverse side if necessary and identify by block number) Experimental and analytical studies were conducted to determine a stall flutter prediction system. The initial phase of work was reported in AFOSR-TR-76-0829 (ADA027869): a second study phase, with an extended range of parameters, is documented in this report AFOSR-TR-77-0854. A series of experimental measurements of airfoil pressure distributions were made in an eleven-airfoil oscillating cascade wind tunnel. The air foils were oscillated in pitch about mid-chord pivots with an amplitude of $\pm 2$ degrees at a tunnel velocity of 200 feet-per-second, obtaining reduced frequencies in the range of 0.03 to 0.20. The incident		

DD FORM 1 JAN 73 1473

EDITION OF 1 NOV 65 IS OBSOLETE

UNCLASSIFIED

SECURITY CLASSIFICATION OF THIS PAGE (When Data Entered)

air angle was set at  $8^\circ$ , the cascade angle was  $35^\circ$  from a fully-closed setting; tests were run at interblade phase angles of zero,  $+5^\circ$ ,  $+10^\circ$ ,  $+20^\circ$ ,  $+30^\circ$ ,  $+45^\circ$ ,  $+60^\circ$ . Sample time histories of pressure and hot film response are discussed in relation to previous OSR/SQUID data, and converted to unsteady pressure, lift and pitching moment coefficients. These data are compared with calculated values obtained from a computational program originated by P V Perumal for unsteady incompressible cascade flow with steady separation. An algorithm was fitted to the experimental coefficients, and used to predict the aerodynamic damping for a case of torsional stall flutter observed in the stator of an existing fan. In this calculation, the algorithm was modified by a compressibility correction obtained as the ratio of a cascade calculation for the desired Mach number to a similar calculation for the Mach number of the algorithmic coefficients, both for unseparated flow. The prediction thus obtained was for unstable operation, but indicated too pronounced an instability. It was tentatively concluded that the flow incidence angle of the present data may be significantly greater than that of the stall flutter example. Tests at lower incidence angle and an increase in the frequency of oscillation are the recommended directions for extended investigations.

to - 60 deg.



to -

UNCLASSIFIED

18 AFOSR-TR-77-0854

6 **ANALYTICAL AND EXPERIMENTAL STUDY  
OF SUBSONIC STALLED FLUTTER,**

10 R. A. /Arnoldi W. N. /Dalton  
F. G. /Carta A. O. /St Hilaire  
R-H /Ni

Pratt & Whitney Aircraft Group  
Government Products Division  
West Palm Beach, Florida 44402

11 31 July 1977

12 59 p.

9 Final Scientific Report, for Period 1 Apr 1975 — 31 May 1977,

15 F44620-75-C-0066

16 2307

17 A4

Prepared for

UNITED STATES AIR FORCE  
OFFICE OF SCIENTIFIC RESEARCH  
Building 410  
Bolling Air Force Base  
Washington, D. C. 20332

ACCESSIBLE for	
YES	V. Le Section <input checked="" type="checkbox"/>
NO	B. H. Section <input type="checkbox"/>
UNCLASSIFIED	<input type="checkbox"/>
CLASSIFICATION	
BY	
DISTRIBUTION/AVAILABILITY CODES	
SPECIAL	
PA	

392 887

mt

## FOREWORD

This Final Scientific Report was prepared by the Pratt & Whitney Aircraft Group, Government Products Division of the United Technologies Corporation under contract F44620-75-C-0066 to the United States Air Force Office of Scientific Research. Lt.-Col. R. Smith was the AFOSR Program Manager. R. A. Arnoldi was the P&WA Program Manager, coordinating the experimental and analytical phases of the study, and collaborating with R-H. Ni, W. N. Dalton, and D. R. Archer, Jr. in the application of experimental data for the purpose of the present investigation. F. O. Carta directed the experimental activities at the United Technologies Research Center, with the assistance of A. St. Hilaire who also supervised the data reduction. Dr. F. Sisto, Professor Mechanical Engineering at Stevens Institute of Technology, was a consultant for the program. A theoretical analysis and computer program, originated by P. V. K. Perumal at Stevens Institute of Technology under Dr. Sisto's supervision, was adapted for comparison with experiment. An Interim Scientific Report (ref. 1) was submitted at the close of the first year of investigation. This Final Report presents data supplementary to that already described and reaches conclusions based on the entire study.



## TABLE OF CONTENTS

Section	Subject	Page
1.0	INTRODUCTION	1
2.0	TECHNICAL BACKGROUND	2
	2.1 Stall Flutter in Gas Turbine Engine Design	2
	2.2 Dynamic Stall and Stall Flutter	3
	2.3 Origin of Present Stall Flutter Study	4
	2.4 Parallel Development	4
	2.5 Retention of Experimental Cascade Effects in Stall	5
3.0	CASCADE STALL FLUTTER TEST FACILITY	6
	3.1 Test Facility and Experimental Procedures	6
	3.2 Calibration Procedures	7
	3.3 Data Reduction and Reduction Procedures	8
	3.4 Operational Improvements Subsequent to Initial Test Program	8
4.0	UNSTEADY AERODYNAMIC ANALYSIS	10
	4.1 Perumal Unsteady Separated Flow Analysis	10
	4.2 Parametric Trends of Calculated Quantities	11
5.0	EXPERIMENTAL DATA	12
	5.1 Range of Test Parameters	12
	5.2 Pressure Data	12
	5.3 Force and Moment Coefficients	13
	5.4 Hot Film Data	15
6.0	COMPARISON OF DATA WITH ANALYTICAL MODEL	17
7.0	APPLICATION OF A STATISTICALLY FITTED ALGORITHM TO AN EXPERIMENTAL CASE OF TORSIONAL STALL FLUTTER	18
	REFERENCES	20



## LIST OF ILLUSTRATIONS

Figure	Title	Page
1	Compressor Map Showing Flutter Boundaries of Four Types of Flutter	21
2	Subsonic Oscillating Cascade Wind Tunnel	22
3	Schematic of Subsonic Oscillating Wind Tunnel	23
4	Blade Nomenclature	24
5	Instrumented Airfoil Prior to Transducer Placement	25
6	Schematic Plan View of Instrumented Airfoil	26
7	Section View Showing Suction Surface Instrumentation	27
8	Instrumented Airfoils	28
9	Four-Bar Linkage to Produce Sinusoidal Motion	29
10	Contour Plot of Wake Rake Traverse (Corrected Flow Condition)	30
11	Chordwise Pressure Distribution ( $V_{REF} = 196.51$ f.p.s.)	31
12	Parametric Variation of Lift Coefficient with Interblade Phase Angle ( $k = .035$ )	32
13	Parametric Variation of Moment Coefficient with Interblade Phase Angle ( $k = .035$ )	33
14	Parametric Variation of Lift Coefficient with Interblade Phase Angle ( $k = .086$ )	34
15	Parametric Variation of Moment Coefficient with Interblade Phase Angle ( $k = .086$ )	35
16	Parametric Variation of Lift Coefficient with Interblade Phase Angle ( $k = .135$ )	36
17	Parametric Variation of Moment Coefficient with Interblade Phase Angle ( $k = .135$ )	37
18	Time-Averaged Wave Forms of Pressure Oscillations at Various Airfoil Chordwise Locations ( $\alpha = +60^\circ$ , $f = 17.1$ c.p.s.)	38

## LIST OF ILLUSTRATIONS (Cont'd)

Figure	Title	Page
19	Time Averaged Wave Forms of Pressure Oscillations for Various Interblade Phase Angles (Airfoil Suction Surface Sensor at 1.2% Chordwise Locations, $f = 17.1$ c.p.s.)	39
20	Time-Averaged Wave Forms of Pressure Oscillations for Various Interblade Phase Angles (Airfoil Suction Surface Sensor at 6.2% Chordwise Location, $f = 17.1$ c.p.s.)	40
21	Variation of Unsteady Pressure Over Airfoil Suction Surface During One Cycle ( $\sigma = 60^\circ$ , $f = 17.1$ c.p.s.)	41
22	Pressure Response of Three L. E. Suction Surface Sensors at Two Interblade Phase Angles ( $f = 17.1$ c.p.s.)	42
23	Time-Averaged Wave Forms on Pressure Surface ( $f = 17.1$ c.p.s., $\sigma = +60^\circ$ )	43
24	Time-Averaged Wave Forms on Pressure Surface ( $f = 17.1$ c.p.s., $\sigma = -60^\circ$ )	44
25	Instantaneous Chordwise Pressure Distribution ( $f = 17.1$ c.p.s., $\sigma = -60^\circ$ )	45
26	Instantaneous Chordwise Pressure Distribution ( $f = 17.1$ c.p.s., $\sigma = +60^\circ$ )	46
27	Comparison of Pressure and Hot Film Response for $\sigma = \pm 60^\circ$ ( $f = 4.5$ c.p.s.)	47
28	Comparisons of Pressure and Hot Film Response for $\sigma = \pm 45^\circ$ ( $f = 4.5$ c.p.s.)	48
29	Comparisons of Pressure and Hot Film Response for $\sigma = \pm 30^\circ$ ( $f = 4.5$ c.p.s.)	49
30	Comparison of Statistical Algorithm and Experimental Data, Moment Coefficient Due to Torsion, Vector Amplitude	50
31	Comparison of Statistical Algorithm and Experimental Data, Moment Coefficient Due to Torsion, Vector Phase Angle	51
32	Fan Exit Guide Vane Stability As Predicted by Empirical Algorithm	52

## SECTION 1.0

### INTRODUCTION

The accomplishment of potential engine design improvements in efficiency, weight reduction and durability, of which our latest technology is capable, is often frustrated by design requirements to avoid flutter. Anti-flutter requirements may be excessive, containing safety margins for unknown factors; however, despite the design margins, an unforeseen effect may result in flutter during engine development. This is particularly true of stalled flutter, for which the available experimental data is insufficiently detailed to allow adequate physical models.

Theoretical analyses have been developed on the basis of hypothesized models and have been applied to flutter prediction, but the fundamental experimental data are insufficient to evaluate the accuracy of the physical model. P&WA and UTRC conducted a series of experiments, under Air Force Office of Scientific Research (AFOSR) auspices, to obtain new data and to evaluate one of these hypothesized models with a view towards its possible validation as a predictive tool. Additional aims were to improve the understanding of dynamic stall, and accumulate a data bank for general use in the field of aerodynamic behavior.

The first year of P&WA investigative work provided data and pertinent analysis for two interblade phase angles and three incidence angles at several tunnel speeds. An Interim Scientific Report was issued (ref. 1), noting good agreement between theory and experiment, and accordingly, a second year of work was authorized. The study was extended to a wider range of interblade phase angles at one incidence angle and single tunnel speed, to further increase the data bank. A direct test of the data bank was accomplished by fitting an algorithm to a case of stator stall flutter in torsion.

This Final Scientific Report, while inclusive of the entire study as a basis for its conclusions, presents data supplementary to that already described in the Interim Report (ref. 1).

## SECTION 2.0

### TECHNICAL BACKGROUND

#### 2.1 Stall Flutter in Gas Turbine Engine Design

Subsonic stall flutter is one of at least four types of flutter that may occur in a compressor rotor. The unsteady aerodynamics associated with each type of flutter differ significantly, and therefore the compressor designer must use a different approach to remove each type from the compressor operating range. Each type of flutter may occur in shrouded or shroudless rotors. The four types of compressor flutter are described in the following paragraphs.

Representative boundaries for each type of flutter are shown on the compressor map, Figure 1. The map depicts a typical compressor operating line intersected by three constant speed lines and bounded at high pressure ratios by the surge line. Flutter "boundaries" on the map are contour lines of constant amplitude flutter stress, and as such, are somewhat arbitrary, depending on the stress level selected to represent the boundary.

1. Subsonic Stall Flutter – This type of compressor flutter is characterized by self-excited blade vibration at operation near the surge line, and may be identified by observing in test data that the flutter stresses increase as the pressure ratio is raised. In a high-speed fan stage, subsonic stall flutter will occur at part-speed operation; in a low-or high-pressure compressor, subsonic stall flutter may occur at or near design speed. It is suspected that during stall flutter, separated flow exists on the compressor blades over at least a portion of a cycle of oscillation.
2. Choke (Negative Incidence) Flutter – This type of compressor flutter is characterized by flutter stresses which occur while a fan is operating either subsonically or transonically. The stresses will increase as pressure ratio is lowered, and experience indicates that during choke flutter, the rotor is operating at near-choke conditions and the flow is transonic over most of the blade chord.
3. Supersonic Stall Flutter – This type of compressor flutter occurs when the outer portion of the blade is operating supersonically, and the stage is operating near the surge line. The flow has strong shocks in the blade passages.
4. Supersonic Unstalled Flutter – This type of flutter occurs when the outer span of the blade is operating supersonically, is somewhat stabilized by increasing back pressure, and can still occur at the design point conditions. This flutter occurs in vibrational modes that are predominantly torsional. The occurrence of this type of flutter imposes a limit on high speed operation.

Subsonic stall flutter in compressors is not a new problem. Around the year 1951 a number of blade failures were reported in axial compressors. They generally occurred in the higher pressure ratio compressors that were then coming into general use. It was observed that changes in blade material and blade frequency seemed to have little effect, and considerable stiffening of the blades was necessary before satisfactory operation could be obtained.



It was concluded by Carter and Kilpatrick (ref. 2), that the failures were due to the blades losing their aerodynamic damping while operating in a higher loaded flow condition. Once the aerodynamic damping became negative, the amplitude of blade vibration increased until it was limited by non-linearity of the damping forces, or the blade broke.

Since that time many compressor stages have failed or been limited in operation by stall flutter. Flutter-prone stages have been redesigned using empirical design rules developed in the hard school of testing. However, as compressor design philosophy has changed to give higher pressure ratio, higher efficiency, and lower weight, old design rules have failed.

Today, many high-speed shrouded and shroudless fan rotors are experiencing torsional mode stall flutter at part-speed operation. No adequate design criteria exist at this time to predict the stall flutter boundary for these fan blades. Clearly, a better understanding of the stall flutter mechanism is needed if the designer is to continue to increase performance while lowering engine weight and maintaining a safe subsonic stall flutter margin.

Because of the development of two new capabilities, it is now possible to initiate a basic research program into understanding the stall flutter mechanism. The new capabilities are supplied by:

- An unsteady, separated flow cascade analysis which accounts for the effects of cascade geometry, reduced frequency, and interblade phase angle, but requires input data on boundary layer separation point position, and
- A cascade tunnel where fully-instrumented airfoils of suitable turbofan cross-section can be oscillated at arbitrary frequency and interblade phase angle while the boundary layer separation point motion and unsteady surface pressures are recorded.

## 2.2 Dynamic Stall and Stall Flutter

Dynamic stall describes a process whereby stalling occurs on an airfoil surface in a transient manner. Since the flow field present during incipient stall flutter in a compressor is that of a cascade of airfoils at an angle of attack near the static stall angle and oscillating at small amplitude (less than one degree) and moderate frequency, it is generally assumed that dynamic stall is present during stall flutter. More importantly, dynamic stall is probably present before the angle of attack (blade loading) is high enough for stall flutter to occur. Also, dynamic stall may be present if the blade frequency is too high to allow stall flutter. The relationship between dynamic stall and stall flutter on an isolated airfoil is described by Carta et al (ref. 3).

Subsonic stall flutter has been a recurrent problem in fans and compressors. It usually occurs near the compressor surge line, and is identified by an increase in flutter stress as pressure ratio is increased at constant speed. There are no experimental data available to indicate whether, at the onset of flutter, the flow is fully attached along the blade suction surface or is separated during either a portion of, or during the entire blade oscillation. However, in cases where the onset occurs close to surge conditions, separation seems likely and attempts have been made to base predictions on observations and theories relating to the existence of



separation. Most of these attempts have been based on isolated airfoil results, ignoring the strong aerodynamic interactions known to exist between adjacent airfoils. These interactions are also known to be strong in the case of unseparated flow, depending on the cascade stagger, the gap-to-chord ratio, the aerodynamic blade loading, and the interblade phase angle associated with a particular vibrational mode.

It is necessary to study the aerodynamics of separated flow on a sequence of blades oscillating with equal amplitudes and equal phase angles between their motions, in order to establish the strength of the interactions where available theory may not be adequate. This was undertaken analytically by Perumal (ref. 4), whose analysis treats a cascade of flat plate airfoils oscillating at uniform interblade phase angle at zero incidence in steady, incompressible flow. The flow is assumed to separate at a fixed location on each blade and the ensuing separation streamline remains parallel to the blade surface, resulting in a separated wake of negligible thickness. The predictions of this analysis have been compared with experiment in the initial phase (ref. 1) of the present AFOSR-sponsored program at P&WA, using an Oscillating Cascade Wind Tunnel developed by the United Technologies Research Center.

While the framework offered by the Perumal theory can be used to present experimental observations on flow separation in a form suitable for analytical study of flutter in separated flow, the analytical model chosen by Perumal is very much idealized and experimental discrepancies may be expected. Predictions of aerodynamic damping, for use as a correlating parameter for flutter data on actual compressors and fans, require various modifications to the model, reducing data scatter on an empirical basis.

The use of such a semi-empirical function for flutter data correlation is part of a unified approach to flutter prediction developed at P&WA during the last several years (ref. 5). The aeromechanical stability of the blade-disk system is expressed in terms of a stability parameter which measures the amount of unsteady work done by the air on the system, when the system is vibrating in one of its natural modes. In neutrally stable systems, the unsteady work done by the air on the blades will balance the work dissipated by rubbing friction and by internal material damping. An accurate prediction of the vibrational deflections and of the unsteady aerodynamic forces is required at every spanwise location on each blade, so that the work done by the unsteady aerodynamic forces may be calculated.

### 2.3 Origin of Present Stalled Flutter Study

The initial dynamic stall study was based on the expectation that the Perumal theory can be used as a primary analytical framework for construction of a semi-empirical unsteady aerodynamic algorithm to be used in stalled flutter prediction. The intention of the second phase of study was to secure a wider range of interblade phase angles to evaluate this expectation, and to devise an independent algorithm which could be used to directly fit the data. This algorithm can then be used in lieu of direct interpolation of the data in the evaluation of stall flutter sensitivity of new blade designs.

### 2.4 Parallel Development

A parallel development has taken place at the P&WA Government Products Division (GPD)

relative to stalled flutter problems encountered during development of the F-100 turbofan engine (ref. 6). GPD aeroelasticians have developed a promising criterion for stall flutter, calculating the aerodynamic damping on the basis of an algorithm incorporating isolated airfoil experimental data (separated flow) to modify otherwise unseparated analytical predictions based on the best available cascade theoretical analyses. While the degree of data correlation from all P&WA cases of stalled flutter is still under scrutiny by both GPD and East Hartford aeroelasticity groups, the general approach used in developing the semi-empirical algorithm appears to have a very favorable chance of success in flutter prediction.

## 2.5 Retention of Experimental Cascade Wake Effects in Stall

A potential improvement over the GPD semi-empirical aerodynamics appears possible if the isolated airfoil data can be replaced by cascade data, thereby retaining the experimental cascade wake effects when the cascade is in stall.

The wakes are known to play a very strong part in the unsteady interaction between the airfoils, especially for highly staggered cascades of low gap-to-chord ratio. Much of the sensitivity of the unsteady aerodynamic coefficients to interblade phase angle is due to this wake effect, and it is important to retain as much as possible of the empirical nature of the resulting mixed flow region in building a semi-empirical algorithm. The wake aerodynamics of an oscillating airfoil is reviewed briefly, as follows, to emphasize the reasons for retaining the stalled wake characteristics.

When the oscillating airfoil experiences a change in lift, the air flowing past its trailing edge is observed to experience a corresponding difference in velocity on either side of the trailing streamline, proportional to the rate of change in lift. This difference in velocity will therefore, exist in the downstream wake as a history of the changes in lift experienced by the airfoil; known as circulation, it is swept downstream with the wake. The circulation has the property of inducing a velocity at all points in the field, including the original airfoil and other airfoils in the cascade. Since the total induced velocity at any point depends on the instantaneous position and strength of all centers of circulation in the flow field, it is important that the wake streamlines be correctly identified and the correct velocity of convection be associated with position along each streamline. This is clearly an exacting requirement even in unseparated flow, and it is impressive that existing theories have proven so effective in unstalled flutter. In the absence of a stalled theory which predicts steady streamline geometry, it is desirable to keep as much as possible of these wake effects in the empirical portion of the desired algorithm.

## SECTION 3.0

## CASCADE STALL FLUTTER TEST FACILITY

## 3.1 Test Facility and Experimental Procedures

Tests have been conducted in a linear, subsonic Oscillating Cascade Wind Tunnel (OCWT) which is illustrated in Figure 2 and shown schematically in Figure 3. The test section of the OCWT is 10 inches wide and 25 inches high, and is presently configured to have 11 shaft-mounted blades in cascade. The bearing mounts for these blades are equally placed along a line making a 30-degree angle with respect to the tunnel floor, hence, the sidewall stagger of the OCWT is nominally 30 degrees. Boundary layer slots are located ahead of the test section on both sidewalls and on the tunnel ceiling and floor. The boundary layer air is evacuated by means of an auxiliary vacuum pump.

The main 10- by 25-inch test section receives its air from atmosphere through an upstream bellmouth and discharges downstream through two Allis-Chalmers centrifugal compressors which are driven by a P&WA FT-12 engine. Inlet angle variations into the test section are obtained by rotating the floor and ceiling nozzle blocks about a pair of pivots whose centers lie along the locus of blade leading edges. Tests are carried out with a fine mesh screen placed over the bellmouth and with an aluminum honeycomb inserted in the rectangular entry region. Neither of these flow straightening devices are shown in Figure 2.

The cascade configuration under test consists of eleven blades, each of which has a chord of  $C = 6$  inches and a span of  $L = 10$  inches. The airfoil has a NACA 65 series profile with 10 degree camber and a thickness-to-chord ratio of 0.06. Figure 4 is a schematic drawing of four of the 11 blades as they are mounted in the wind tunnel. The relative positions are scaled properly but the blade shapes have been exaggerated for clarity in describing the blade shape parameters. The slant gap, measured along the blade-to-blade stagger line is  $\tau = 4.5$  inches so the gap-to-chord ratio is  $\tau/c = 0.75$ .

For the series of test points reported herein, the blade chordline coincides with the horizontal datum, and hence the chordal stagger angle  $\alpha_{CH}$  is  $35^\circ$ , and the tunnel sidewall stagger angle,  $\theta_{SWS}$ , is  $30^\circ$ .  $\alpha_{CH}$  was changed from a previous value of 30 degrees, held during the test runs reported in ref. 1. The data are not a strong function of this angle, and it was anticipated that improved distribution of steady flow would result. The blade stagger angle,  $\beta_1^*$ , is measured between the tangent to the blade mean camber line at the leading edge and the leading edge locus line. Note that this angle is the complement of NASA definition of blade angle. Finally, the blade inlet angle,  $\beta_1$ , is measured between the inlet velocity  $V$  and the leading edge locus line.

At this point it is convenient to introduce some definitions relating the airflow direction to the blade orientation. First, if it is assumed that the free stream velocity is parallel to the upstream nozzle direction, then the velocity vector makes an angle  $\theta_N$  relative to the horizontal datum. Hence

$$\beta_1 + \theta_N = \theta_{sws}$$



and in this test, with  $\theta_{\text{sws}} = 30^\circ$  and  $\alpha_{\text{CH}} = 35^\circ$

$$\beta_1 + \theta_N = 30 \text{ deg.} \quad (2)$$

Now define the angle of incidence relative to the mean camber line as

$$\alpha_{\text{MCL}} = \beta_1^* - \beta_1 \quad (3)$$

It was stated earlier that these airfoils have  $10^\circ$  of camber distribution over a circular arc mean camber line. Hence the departure of the mean camber line from the chord line will be equally distributed as  $5^\circ$  at both leading and trailing edges, or  $\alpha_{\text{CH}} - \beta_1^* = 5^\circ$  and with  $\alpha_{\text{CH}} @ 35^\circ$ , then  $\beta_1^* = 30^\circ$ . Hence, from equations (2) and (3),

$$\alpha_{\text{MCL}} = \theta_N$$

The center airfoil of the cascade is heavily instrumented with both miniature high response pressure transducers and with hot film transducers. This blade is illustrated in Figure 5 prior to the insertion of the pressure transducers, and is shown schematically in Figures 6 and 7. Figure 6 shows the permanent locations of all pressure orifices and the array of hot films at the leading edge region used in the first series of tests. Figure 7 shows the method used to insert the high response pressure transducers into the airfoil. Figure 8 illustrates the suction surfaces of two instrumented blades currently in use.

The entire set of airfoils is driven coherently in a sinusoidal pitching motion with an amplitude of  $\alpha = \pm 2$  degrees. The system is driven by an electric motor through a series of timing belts and pulleys, as shown in Figure 3. The direct drive to each blade culminates in a four bar linkage, shown in Figure 9, which provides a sinusoidal motion with low harmonic distortion.

### 3.2 Calibration Procedures

Prior to testing, all pressure transducers were individually calibrated. A vacuum line was applied to each location and the diaphragm of each transducer was cycled through a sequence of pressures down to approximately 33 inches of water below atmospheric pressure and back again. The output voltage for each imposed pressure point was recorded, and similarly, the output voltage for an imposed calibration resistor was recorded. The product of the slope of the calibration curve, in p.s.i./volt, and the output due to the calibration resistor, in volts, yielded an equivalent pressure in p.s.i., dependent only on the calibration deflection and invariant with transducer excitation.

A simple voltage calibration was also performed on each hot film during this sequence of tests. Although this was not meaningful in absolute terms, (cf, the discussion on relative hot film measurements in ref. 7), the calibration allowed relative comparisons between the outputs of the various films and between the hot film responses from run to run.

### 3.3 Data Acquisition and Reduction Procedures

Time history data from the instrumentation described earlier is stored on FM magnetic tape during the test and is subsequently processed. This has a number of advantages: 1) it permits the test to proceed without interruptions required to perform on-line data reduction; 2) a single section of stored data can be processed by a variety of techniques and the results compared; and 3) the use of a multispeed tape recorder can enhance the ability of the investigator to examine both low and high frequency phenomena.

The system being used is referred to as the Wideband System for Acquiring and Recording Data (WISARD). In its acquisition mode, the WISARD normally takes voltage data from the transducers (pressure, hot film, and capacitive airfoil position transducers), passes it through signal conditioners, amplifiers (where necessary), filters and thence onto a multi-channel FM magnetic tape. Data recording takes place at any of a number of selected tape speeds, from 1-7/8 i.p.s. to 120 i.p.s. Playback is restricted to 1-7/8 i.p.s. This operating flexibility makes it possible to maximize the frequency resolution of each unsteady signal, regardless of the oscillatory frequency. By this means it is possible to obtain test information at higher frequencies than would otherwise be possible if recording and playback speeds were equal.

During playback, the multichannel data are processed by a multiplexer, a sample-and-hold register, and an analog-to-digital converter. The resulting digitized information is transferred to a digital tape for subsequent processing on a large digital computer. The basic output information consists of integrated lift, moment, pressure and airfoil position time histories, lift and moment hysteresis loops, and hot film time history response. Derived results can include spectral or Fourier Analysis of the unsteady data, dynamic pressure wave analysis, and correlations of pressure data with hot film data.

During the current test program, the system has been improved by insertion of a preamplifier between the transducer and the signal conditioner. This provides isolation from inherent system noise and has an initial gain of 100. Hence, the instrumentation amplifier gain need only be 10, and the signal to noise ratio is enhanced accordingly. In addition, the preamplifier can be operated as a DC coupled system, which passes steady state signals for calibration, and as an AC coupled system, which suppresses all DC signals including long term thermal drift. In this type of operation, the zero reference condition is obtained from the static pressure tap readings of the blade through long pneumatic tubes and a manometer system.

The hot-film response is obtained through a set of constant temperature anemometers whose outputs are recorded directly onto the FM magnetic tape. Although these results are only qualitative (i.e., no absolute magnitudes may be ascribed to any of the output signals), a great deal of valuable information can be obtained from them.

### 3.4 Operational Improvements Subsequent To Initial Test Program

The OCWT was subjected to comprehensive aerodynamic survey to ascertain the degree of flow uniformity upstream of the cascade and to determine whether the desired levels of aerodynamic loading across the cascade were being achieved. All testing reported herein was performed at a mean flow velocity of 200 f.p.s. and an incidence angle to the mean camber line of eight degrees.



#### PRATT & WHITNEY AIRCRAFT GROUP

Three major problem areas were defined and corrected. The first problem involved a total pressure distortion introduced by a honeycomb flow-straightener installed at the tunnel inlet. This distortion, with a magnitude of approximately 30 percent of the tunnel dynamic head, was introduced by irregularities in manufacture and misalignment in installation. A new piece of higher quality honeycomb material was installed in precise alignment with the flow direction. Further surveys revealed minimal distortion level, well within the general turbulence level of the facility. A second area of concern was the sidewall boundary layer removal system, which was failing to remove some portion of the boundary layer near the tunnel floor. Measurements along the length of the collection plenum revealed a static pressure gradient, indicating flow was stagnating in the region of the floor. Additional honeycomb was added in the plenum to remove this problem. A third problem area was leakage of flow around the blade support shafts. As much as three percent additional flow was capable of leaking through this area, causing a flow skew at the wall. Teflon pads were added as seals to correct this problem.

A complete wake survey was taken and a contour plot of the pressure field down-stream of the cascade was made (Figure 10). The contour plot shows a large area of clean flow about the midspan. At the point where the vane and wall meet, a corner vortex forms and is swept downstream. A chordwise pressure distribution is shown in Figure 11. A static pressure rise coefficient of .366 was achieved. Wedge probe data indicates the air is turned  $11.3^\circ$ .

A comparison was made between measured cascade performance and performance predicted by the P&WA cascade correlation system. The cascade correlation indicates a turning angle of  $11.5^\circ$  with a static pressure rise coefficient of 0.48. Thus the desired turning was achieved, but at a lower static pressure ratio. The deviation of the measured static pressure coefficient from the desired value is due to the three-dimensional effects incurred by the existence of the wall vortices which cause an added loss of total pressure at the wall, resulting in a lower possible static pressure rise.

## SECTION 4.0

### UNSTEADY AERODYNAMIC ANALYSIS

#### 4.1 Perumal Unsteady Separated Flow Analysis

A series of unsteady separated flow analyses had previously been constructed under the leadership of Dr. F. Sisto of the Stevens Institute of Technology. The latest analysis in the series includes cascade interactions of airfoils, and was made by Perumal (ref. 4), using the methods of conformal transformation to map the geometric boundaries (including the separation streamlines) into the abscissa of the transformed plane. An acceleration potential solution in this plane is then found, which is subsequently transformed back to the physical plane. The assumptions involved in this solution are as follows:

1. The cascade airfoils are flat plates and all steady streamlines are straight lines parallel to the airfoil surfaces. This precludes any variation in unsteady aerodynamics which might be caused by steady loading (flow turning);
2. The separation streamlines originate from fixed points at identical chordwise locations on each airfoil. It was not found possible to accommodate any chordwise oscillation of these points if the desired condition of non-zero interblade phase angle was to be retained;
3. The perturbation pressure is zero in the separated regions at all times; and
4. No compressibility effects have been included.

These restrictions were considered to require experimental evaluation before the analysis could be rationally applied to stall flutter prediction in fans or compressors. In addition, it was anticipated that Perumal would be able to complete the removal of the second restriction, and that data on separation point motion could be directly incorporated in the analytical applications. This proved unduly optimistic; only the location of separation and not its motion is available as a parameter for matching data to analysis.

The Perumal unsteady cascade theory considers small perturbations about the two-dimensional, steady flow of an incompressible, inviscid fluid over an infinite linear cascade of flat plates. The plates are undergoing harmonically time-dependent motions of small amplitude with constant interblade phase ( $\sigma$ ). The flow is assumed to be partially separated on the suction surface of the plates, and the wakes are taken to be straight slits extending from the separation point to downstream infinity. A linearized solution satisfies the boundary conditions at the fixed wake-slits, representing the mean position, rather than the instantaneous position, of the oscillating plates. The pressure is assumed constant in the separated regions of the slits and in the wakes. At other regions of the slits, the vertical components of both velocity and substantial acceleration of the fluid are matched respectively to the appropriate functions of oscillating blade displacement.

Further constraints which are satisfied in the solution are the continuity of the complex acceleration potential at the trailing edges (Kutta condition), and at the separation points, and

the requirement that the pressure perturbations die off at inlet conditions. The acceleration stream function is obtained as the sum of an infinite series of integrals (one for each blade) of the unknown acceleration potential function. Since the value of the acceleration stream function on the blade surface is given, the unknown acceleration potential (and thus the perturbation pressure) can be found by solving the resultant singular integral equation.

Due to the assumption of constant pressure after the separation point and in the wake, the solution obtained for the case of a trailing-edge separation point cannot be compared, in general, with the unseparated flow solution of Smith (ref. 8). However, under the conditions of zero or  $180^\circ$  interblade phase angle at zero stagger, the unseparated theory (ref. 8) does predict zero perturbation pressure in the wake, and the aerodynamic coefficients computed by both theories show significant agreement.

#### 4.2 Parametric Trends of Calculated Quantities

The Perumal calculation procedure was developed for the PDP-10 computer system, and adapted to the IBM 370-168 system at P&WA with certain numerical modifications. Calculated values were compared with experimental results of the first phase of this program (ref. 1).

The Perumal theory exhibited parametric trends that were generally consistent with the experimental results if a separation point location were assumed for best fit; however, enough discrepancies existed so that the present phase of the program was designed to secure an algorithm as a statistical fit to the data. It was still desired to compare the Perumal calculation results with the new data, particularly relative to the parametric trend of interblade phase angle.

These parametric trends with interblade phase angles are shown in Figures 12 through 17, calculated for assumed separation at .75 chord (the recommended assumption for best general fit) and also at .50 chord for comparison. It may be seen that the general feature consists of instability for positive interblade phase angles and stability for negative values, both in calculated and in experimental results. (Aerodynamic instability is represented by positive imaginary component of the pitching moment  $C_M$ ). The experimental data are included here both for ready comparison and for future reference.

## SECTION 5.0

## EXPERIMENTAL DATA

## 5.1 Range of Test Parameters

The experiments described in this report were performed at a tunnel velocity of 200 f.p.s., an incidence angle  $\alpha_{MCL} = 8^\circ$ , and frequencies of 4.5, 11.0 and 17.1 c.p.s. yielding reduced frequencies of 0.035, 0.086 and 0.134. Interblade phase angles of  $0^\circ$ ,  $\pm 5^\circ$ ,  $\pm 10^\circ$ ,  $\pm 20^\circ$ ,  $\pm 30^\circ$ ,  $\pm 45^\circ$  and  $\pm 60^\circ$  were covered.

## 5.2 Pressure Data

An arrangement of examples of averaged cyclic waveforms of pressure oscillations on the suction surface is shown in Figure 18 for comparison with similar raw wave forms (ref. 1). The waveform of the sensor closest to the leading edge (L. E.) possesses the same high proportion of second harmonic component that was previously found to be characteristic of  $12^\circ$  incidence but lacking at  $10^\circ$  and  $8^\circ$  in the earlier tests.

It is now known that an inlet distortion was present during these earlier tests (cf. Section 3.4) and it appears that data originally believed to be taken at  $12^\circ$  were actually closer to the  $8^\circ$  data obtained in the present program.

Similar waveforms for a range of interblade phase angles (Figure 19) show the change in harmonic content with variations in interblade phase angle. For the intermediate range of negative interblade phase angles ( $-30^\circ \leq \sigma \leq -10^\circ$ ) the dominant component of the L.E. response is the fundamental harmonic; however, a significant higher harmonic contribution is also present. For extreme values of negative interblade phase angle (cf. Figure 21 for  $\sigma = -60^\circ$ ) and for values of  $\sigma$  greater than  $-5^\circ$ , the major component of the signal is second harmonic. This is considered to be one of the outstanding features of the experimental data.

A secondary effect closely allied to this feature is shown in Figure 20, presenting cyclic waveforms of the second sensor from the L.E. over a range of interblade phase angles. As the phase angle becomes less negative and the second harmonic content of the L.E. sensor increases as in Figure 19, there is an abrupt transition in timing and magnitude of the peak suction experienced by the second sensor. At  $-5^\circ$  phase angle, it increases in magnitude and shifts forward to the end of the first quarter of the cycle.

Another unusual feature of the data, as shown in Figure 21, consists of the waveforms at the extreme negative value ( $-60^\circ$ ) of interblade phase angle at successive chordwise locations of pressure sensors. The L.E. sensor develops a steep drop of suction pressure at about mid cycle. The suction has continued to build up well past the peak of incidence angle (which occurs at the quarter point) and drops in a catastrophic manner, the time of its drop corresponding to a downstream convection approximately equal to the free stream velocity. It may be noted in Figure 20 that the second sensor from the L.E. shows a similar drop at the more negative values of phase angle. The alleviation of the catastrophic loss of suction



pressure at less negative phase angle permits the pressure to return to a more normal timing in respect to peak incidence angle. The waveforms of the first three pressure sensors are shown in Figure 22 for phase angles on either side of the critical phase angle for this return.

The pressure waveforms of the pressure surface sensors are shown in Figures 23 and 24 for extreme positive and negative phase angles. These waveforms are seen to be consistent with the idea that the catastrophic suction pressure drop is due to some passage phenomenon which simultaneously affects the pressure surface. A logical suggestion for such a phenomenon is a strong vortex fed from L.E. separation which breaks loose at half cycle and convects downstream.

The instantaneous chordwise pressure distribution on the suction surface is shown in Figure 25 as the catastrophic slide in suction pressure passes downstream at half-cycle and the L.E. pressure rapidly builds up. The contrast with the similar but lesser slide at .30 cycle in the  $+60^\circ$  phase angle data is shown in Figure 26.

### 5.3 Force and Moment Coefficients

The pressure difference distribution was obtained from measured data at the various pressure transducer locations along the chord. The transducer arrangement was chosen to allow the numerical integrations to be performed using a ten-point Gaussian quadrature scheme over the forward 91 percent of the chord. A three-point interpolation through the data, at  $x/c = .86, .91$ , and through  $\Delta p = 0$  at the trailing edge, was used to complete the integration.

After the chordwise integrals of the unsteady pressure time histories were evaluated, the results were rewritten in non-dimensional coefficient form by using the expressions

$$C_N = \frac{N}{\frac{1}{2} \rho V^2 c}$$

and

$$C_M = \frac{M}{\frac{1}{2} \rho V^2 c^2}$$

The resulting time histories,  $(C_N(t) \text{ and } C_M(t))$ , were largely repeatable; however, a combination of low level noise and random response (the latter during stalled flow) caused some discrepancies to occur from cycle to cycle. Therefore, a time averaging procedure over five cycles was employed for each test point.

The experimental oscillating force and moment coefficients, based on the first harmonic of the averaged waveform of surface pressure, are tabulated in Table I. These coefficients were previously shown as two-dimensional vectors in Figures 12 through 17 in comparison with corresponding values calculated by the Perumal procedure. In regard to vibrational modes encountered in practice, one may observe that the imaginary parts of all moment vectors are positive for all interblade phase angles greater than  $+20^\circ$  and negative for all angles less than  $+20^\circ$ . In relation to stability, the aerodynamic moments therefore all do positive work on the torsional motion at phases greater than  $20^\circ$  and are unstable in purely torsional motion.

TABLE I  
EXPERIMENTAL LIFT AND MOMENT COEFFICIENTS

$V_{\infty} = 200 \text{ f.p.s.}$		$\alpha_{MCL} = 8^{\circ}$				
Freq. (c.p.s.)	$\sigma$ Deg.	$C_N$		$C_M$		k
		Mag.	Phase	Mag.	Phase	
4.5	-60	.0638	2.61°	.0201	-15.55	.035
4.5	-45	.0474	12.04	.0177	-10.42	.035
4.5	-30	.0441	26.39	.0176	- 5.87	.035
4.5	-20	.0352	31.16	.0148	- 5.05	.035
4.5	-10	.0317	24.38	.0148	- 6.98	.035
4.5	- 5	.0282	37.36	.0126	- 2.73	.035
4.5	0	.0227	24.99	.0120	- 8.60	.035
4.5	5	.0182	16.25	.0112	- 9.29	.035
4.5	10	.0181	16.34	.0110	- 4.16	.035
4.5	20	.0145	14.42	.0086	- 0.33	.035
4.5	30	.0231	20.79	.0106	14.17	.035
4.5	45	.0434	21.48	.0155	21.12	.035
4.5	60	.0621	15.69	.0191	15.49	.035
11.0	-60	.1191	0.48	.0337	-16.02	.086
11.0	-45	.1061	- 1.03	.0331	-21.06	.086
11.0	-30	.0848	- 5.14	.0277	-30.54	.086
11.0	-20	.0596	0.48	.0204	-28.70	.086
11.0	-10	.0377	3.35	.0153	-33.27	.086
11.0	- 5	.0294	20.72	.0109	-25.62	.086
11.0	0	.0238	34.02	.0091	-17.24	.086
11.0	5	.0226	33.83	.0089	-13.72	.086
11.0	10	.0191	45.21	.0082	- 1.40	.086
11.0	20	.0286	52.25	.0098	16.59	.086
11.0	30	.0417	44.03	.0136	21.10	.086
11.0	45	.0526	28.61	.0159	16.84	.086
11.0	60	.0620	20.48	.0171	13.55	.086
17.1	-60	.1340	-24.84	.0397	-38.14	.134
17.1	-45	.0899	-29.59	.0304	-54.64	.134
17.1	-30	.0422	-24.38	.0171	-59.84	.134
17.1	-20	.0253	4.54	.0106	-45.76	.134
17.1	-10	.0269	42.59	.0093	-23.52	.134
17.1	- 5	.0406	53.81	.0105	0.0	.134
17.1	0	.0395	53.45	.0111	1.03	.134
17.1	5	.0402	49.94	.0119	5.81	.134
17.1	10	.0366	53.79	.0110	7.84	.134
17.1	20	.0454	51.72	.0124	15.38	.134
17.1	30	.0490	41.69	.0135	14.55	.134
17.1	45	.0586	34.99	.0157	17.86	.134
17.1	60	.0750	28.17	.0194	18.06	.134

#### 5.4 Hot Film Data

The hot-film transducer is basically a resistance thermometer element which reacts to local heat transfer in adjacent fluid. The unit contains a constant-temperature anemometer to complete the bridge circuit, and to provide all necessary control functions. The simplest application of a hot-film transducer reveals changes in surface flow behavior through changes in heat transfer. As the heat transfer from the film to the surrounding fluid changes, the voltage required to maintain constant temperature also changes. The resulting bridge unbalance is recorded on FM magnetic tape and is then digitized and processed by a digital computer.

Transition from laminar flow to turbulent flow is detected by a hot-film transducer as an increase in heat transfer and as an increase in high frequency content of the signal. Turbulent flow is more efficient in mixing the fluid near the surface, and can carry heat away from the surface more readily than a laminar flow. If the flow subsequently separates, the expected mean level of heat transfer will diminish because of the pockets of stagnant fluid which occur in a separated flow. In addition, the occasional random breakaway of heated stagnant fluid from the surface and its replacement by cooler fluid will cause large fluctuations in the hot-film response. Experience has shown that a pattern of surface flow events can only be established with any certainty after a qualitative correlation of signal response with known behavior, preferably by a combination of hot-film response measurements and visualization of the surface flow using oil, smoke, etc.

Previous testing had included hot-film sensors at 15, 40, 60, 80 and 95 percent chord locations. Subsequent sensor deterioration caused failure of all hot-films except those at 15 and 40 percent chord. All hot-films are located on the suction surface.

The hot film data presented in this report are time averaged values over several cycles of oscillation. Data interpretation will be made through comparisons of adjacent hot film and pressure transducer response over 1 cycle of oscillation. The hot film sensor selected for detailed study was located at 15% chord while the two pressure transducers were located at 14.8% and 26.1% of chord. Figure 27 shows hot film response at the two extreme values of interblade phase angle ( $+60^\circ$  and  $-60^\circ$ ). For  $\sigma = -60^\circ$ , the pressure transducer at 14.8% chord shows a strong suction peak beyond the maximum incidence angle followed by a sudden and dramatic increase in pressure. As the pressure is decreasing to a minimum, the hot film indicates strong turbulence to be present. As the pressure reaches its minimum, the hot film shows a corresponding maximum. This response peak is indicative of a corresponding velocity increase. The pressure transducer downstream of the hot film shows a similar response. There is a considerable time lag between the two forward transducers and the sensor at 26.1%. The suction peak for the rearward Kulite occurs as the airfoil passes through zero incidence on its way to its maximum negative excursion. This behavior indicates that an upstream occurrence is convected past these three sensors. The hot film data appears to support the previous interpretation of a vortex sweeping downstream from the leading edge. For a  $+60^\circ$  interblade phase angle, the response plots show a less marked phenomenon. The forward pressure transducer sees peak suction about  $20^\circ$  before maximum incidence and the fall off is much less dramatic. The hot film indicates a large increase in velocity at about the

**PRATT & WHITNEY AIRCRAFT GROUP**

time of the local pressure minimum, followed by highly turbulent flow. The downstream pressure sensor shows a similar response to its upstream neighbor, but with a time delay. These response patterns again suggest that an event is swept past all three sensors. Thus the effect of changing interblade phase angle is to introduce a phase shift in the pressure with respect to the motion. This phase shift alone is sufficient to alter system stability. Two other sets of interblade phase angles are presented ( $\pm 45^\circ$ ,  $\pm 30^\circ$ ) in Figures 28 and 29. These angles show similar trends to the  $\pm 60^\circ$  cases discussed above; however, as the interblade phase angle approaches zero, the magnitude of the response decreases. The reduction in vorticity strength indicates that the event which produced the vorticity is also of reduced strength. This suggests that a further effect of interblade phase angle is to alter the degree to which the airfoil is stalled.



## SECTION 6.0

## COMPARISON OF DATA WITH ANALYTICAL MODEL

It had been anticipated that hot film and pressure data would identify separation location and its possible variation with time. This was in fact obscured, and the match of theory to experiment was finally accomplished on a heuristic basis, i.e., finding what assumption of fixed separation point secured the best data fit. Although a matrix of theoretical calculations had been made early in the program for a wide spread of assumptions regarding separation point locations, it was necessary to supplement these during the actual data fitting procedure. On the experimental side, the hot-film locations were modified as the developing evidence failed to show the initial expectation of a separation point on the forward half-chord with only minor oscillations. The final conclusion was that where the Perumal theory applies, hot-film and pressure transducer evidence fails to indicate separation.

During previous study (ref. 1) significant motion of the separation point was observed at the highest incidence angle ( $\alpha_{MCL} = 12^\circ$ ): it was also observed that the leading edge suction surface pressure showed greatly-increased second harmonic content. In contrast, the corresponding locations at  $\alpha_{MCL} = 10^\circ$  and  $8^\circ$  showed negligible amounts of second harmonic pressure response. The conclusion was that the Perumal theory with fixed separation point should not be used for the highest incidence angle, since the assumptions of its formulation conflict too severely with the observed behavior.

The choice of an effective separation point for data match at  $10^\circ$  and  $8^\circ$  incidence angle was made primarily on the basis of the imaginary part of the predicted moment, since it controls the degree of aerodynamic instability. The real part of the moment, as well as the magnitudes of both the normal force and the chordwise pressure, were considered to be minor factors, primarily on the basis of the predominance of the leading edge pressure oscillation as previously described. On this basis, the best fit was considered to require a 0.75 separation point for  $45^\circ$  interblade phase angle, and a .85 separation point for the  $0^\circ$  interblade phase angle.

In the continuation of the study of a wider range of interblade phase angles, the lift and moment coefficient data in Figures 12 through 17 show a general agreement with theoretical calculations for the positive range of interblade phase angles, if the separation point is assumed to be at .75 chord, but no agreement in the negative range.

While no physical interpretation of this disagreement can be offered at this time, it is felt that some essential portions of a proper model must be lacking. The general argument for positive phase angles in terms of amplitude of the imaginary component and trend with reduced frequency is broken in places by minor discrepancies, but is still sufficiently strong to make the contrasting behavior at negative phase angles significant. The real parts of the experimental coefficients are underpredicted by theory in all cases, but this is not unreasonable when it is noted that the steady flow components depart from the Perumal model.

The only physical observation relevant to this contrasting behavior is the stronger harmonic content of the leading edge pressure sensor waveform at negative interblade phase angles (Fig. 19). However, the waveform at large positive phase angles contains nearly as strong harmonics, so that the argument of theory and experiment in this range must relate primarily to the remaining portions of the airfoil surface.

## SECTION 7.0

APPLICATION OF A STATISTICALLY-FITTED ALGORITHM TO  
AN EXPERIMENTAL-CASE OF TORSIONAL STALL FLUTTER

To determine if test data was directly applicable to design problems, an algorithm for the experimental data was generated. A computational routine using statistical regression techniques was used to fit a surface to the moment coefficient as a function of reduced frequency ( $k$ ), and interblade phase angle ( $\sigma$ ). The curve fitting procedure was applied only to the positive interblade phase angles, due to discontinuities in the shape of the data, around zero interblade phase angle. The algorithm thus generated still remains relevant since all instances of torsional stall flutter in rotors have involved positive interblade phase angles.

The resulting algorithm is a polynomial equation for the vector magnitude and phase angle of the moment coefficient in terms of the independent variables:

$$C_M = (1.392 \times 10^{-5}) \sigma^2 + (8.29 \times 10^{-4}) \sigma + (9.115 \times 10^{-2}) k^2 + .007916$$

$$\Phi_{CM} = -24.143 + 151.62k + 1.631 \sigma - .0157\sigma^2 - 2.908\sigma k$$

where  $\sigma$  is in degrees and  $k$  is the non-dimensional reduced frequency. A comparison of the values generated from the algorithm at the experimental values of  $k$  and  $\sigma$  and the original data is shown in Figures 30 and 31. The data was fitted for the positive range of  $\sigma$  (above  $5^\circ$ ) and not for the negative range due to the marked change in behavior at this point, and to the lack of experimental flutter data at negative  $\sigma$  for comparison. It should be noted that the various polynomial terms in the algorithm are not subject to any physical interpretation, i.e., inertial, damping or stiffness effects. The fit of the data is shown in Figures 30 and 31, from which it is evident that closer correspondence exists at higher  $k$  than in the lower range. Since the application (as will be seen below) uses  $k = .33$  and  $\sigma = 18.95^\circ$ , the extrapolation in  $k$  is the principal uncertainty. The data fit to the algorithm for  $C_M$  (moment amplitude) is good throughout while the fit for  $\phi_{CM}$  is good only for  $k = .134$ . Nevertheless, the algorithm is believed to offer the most practicable means of extrapolating the data. To determine the usefulness of the above algorithm, it is necessary to compare results from it with experimental experience. The case chosen for this purpose was the variable incidence cantilevered exit guide vane (pinned tip) of a two-stage research fan rig which exhibited a torsional mode flutter while the rig was operating in a highly loaded condition. The subject vane was a 65 series circular arc meanline airfoil. The camber angle varied from  $64^\circ$  at the root to  $49^\circ$  near the tip. The average thickness ratio was .075. There were 76 vanes in the pack. Onset of flutter occurred at  $M = 0.62$  in a vibrational mode at  $k = 0.33$ . Since the motion was purely torsional, only the imaginary component of the moment coefficient contributes to the system aerodynamic damping. A negative value of this component indicates an unstable system (flutter) unless there is sufficient mechanical damping to dissipate the energy absorbed from the air. For purposes of this report, a zero value of the imaginary moment coefficient was considered the incipient flutter condition. Similarly, since the flutter mode was a single degree of freedom vibration, the value of the imaginary moment coefficient at a single station on the airfoil is sufficient to define system stability.

Following the above reasoning, the previously determined algorithm was applied to the test case for a single station near the vane tip where the torsional amplitude would be a maximum. To apply the algorithm to this particular problem requires using the equations in a region of reduced frequency well beyond the region in which the original data was acquired. Furthermore, it is necessary to arrive at a Mach number correction for the algorithm since the original data were taken in nearly incompressible flow. The Mach number correction factor was arrived at by using the unloaded flat plate cascade analysis (ref. 8). The ratio of the imaginary moment coefficient at  $M=0$  and  $M=0.62$  was formed and applied directly to the coefficient from the algorithm. Using the above correction, aerodynamic damping for the test case was predicted to show a variation with interblade phase angle as given by Figure 32. The minimum at  $18.95^\circ$  phase angle would correspond to four nodal diameters, so that flutter would be expected to occur in a four-nodal diameter mode.

The large negative value of the predicted aerodynamic damping coefficient appears to be too strong in view of the experimental condition consisting of flutter onset. It appears natural to suspect that the steady flow incidence angle is too great, and tests at lower incidence would be desirable (in addition to the extended frequency range mentioned above) in any extension of this work.

## REFERENCES

1. Arnoldi, R. A., F. O. Carta and R. H. Ni: "Analytical and Experimental Study of Subsonic Stalled Flutter", AFOSR-TR-76-0829 (ADA027869) May 1976.
2. Carter, A. D. S. and D. A. Kilpatrick: Self-Excited Vibration of Axial-Flow Compressor Blades. Proceedings of the Institution of Mechanical Engineers, Vol. 171, 1957, pp. 245-281.
3. Carta, F. O., G. L. Commerford, R. G. Carlson, and R. H. Blackwell: Investigation of Airfoil Dynamic Stall and its Influence on Helicopter Control Lodds. USAAMRDL Technical Report 72-51, U. S. Army Air Mobility Research and Development Laboratory, Fort Eustis, Virginia, September 1972.
4. Perumal, P. V. K., "Thin Airfoil in Eddy-Array & Part-Stalled Oscillating Cascade," PhD Dissertation, Stevens Institute of Technology, Hoboken, New Jersey, 1975.
5. Mikolajczak, A. A., et al: "Advances in Fan and Blade Flutter Analysis And Predictions". AIAA Journal of Aircraft, April 1975, pp. 325-332.
6. Jeffers, J. D. II, and C. E. Meece, Jr., "F100 Fan Stall Flutter Problem Review And Solution". AIAA Journal of Aircraft, April 1975, pp. 350-356.
7. Carta, F. O. and A. O. St. Hilaire, "An Experimental Study On the Aerodynamic Response of a Subsonic Cascade Oscillating Near Stall" Project SQUID Technical Report, UTRC-2-PU, July 1976.
8. Smith S. N., "Discrete Frequency Sound Generation in Axial Flow Turbomachines," Report CUED/A-Turbo/TR29, 1971, University of Cambridge, England.



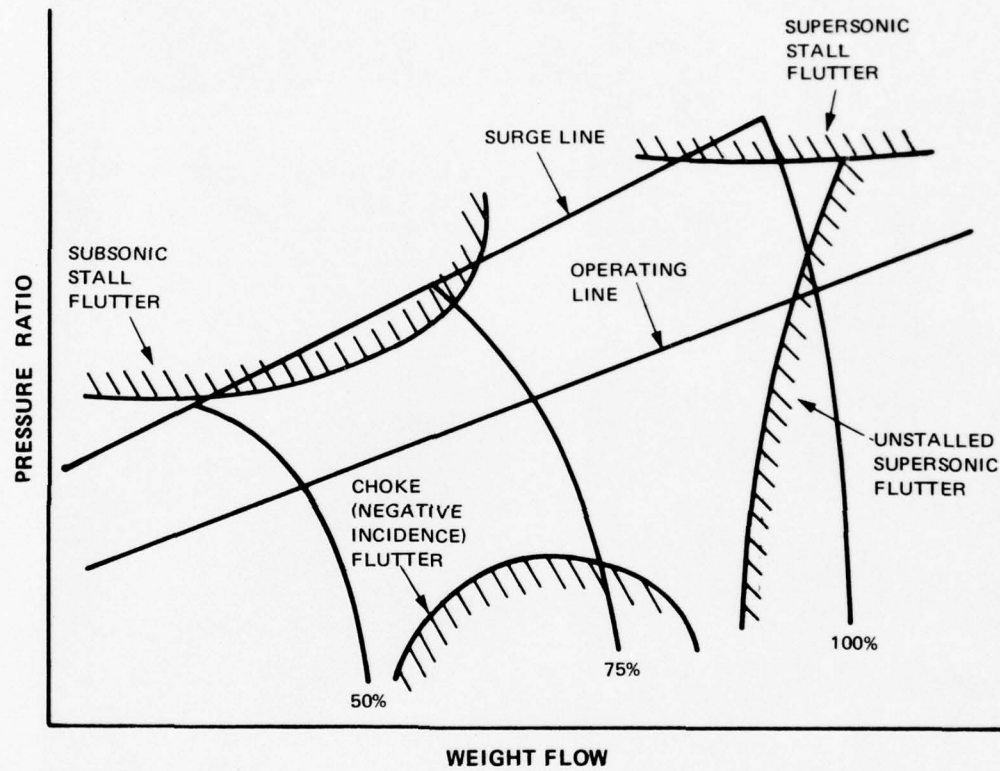


*Figure 1 Compressor Map Showing Flutter Boundaries of Four Types of Flutter*

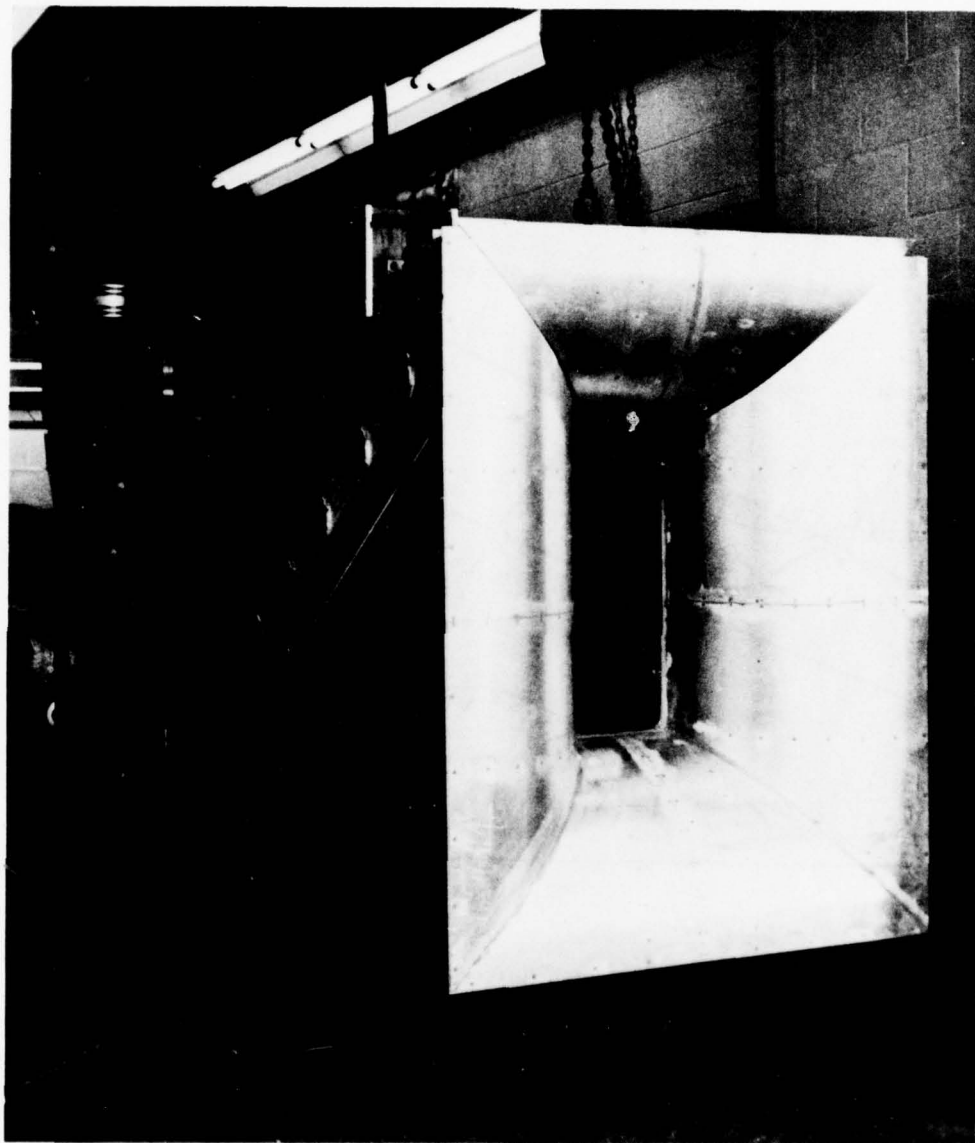


*Figure 2 Subsonic Oscillating Cascade Wind Tunnel*

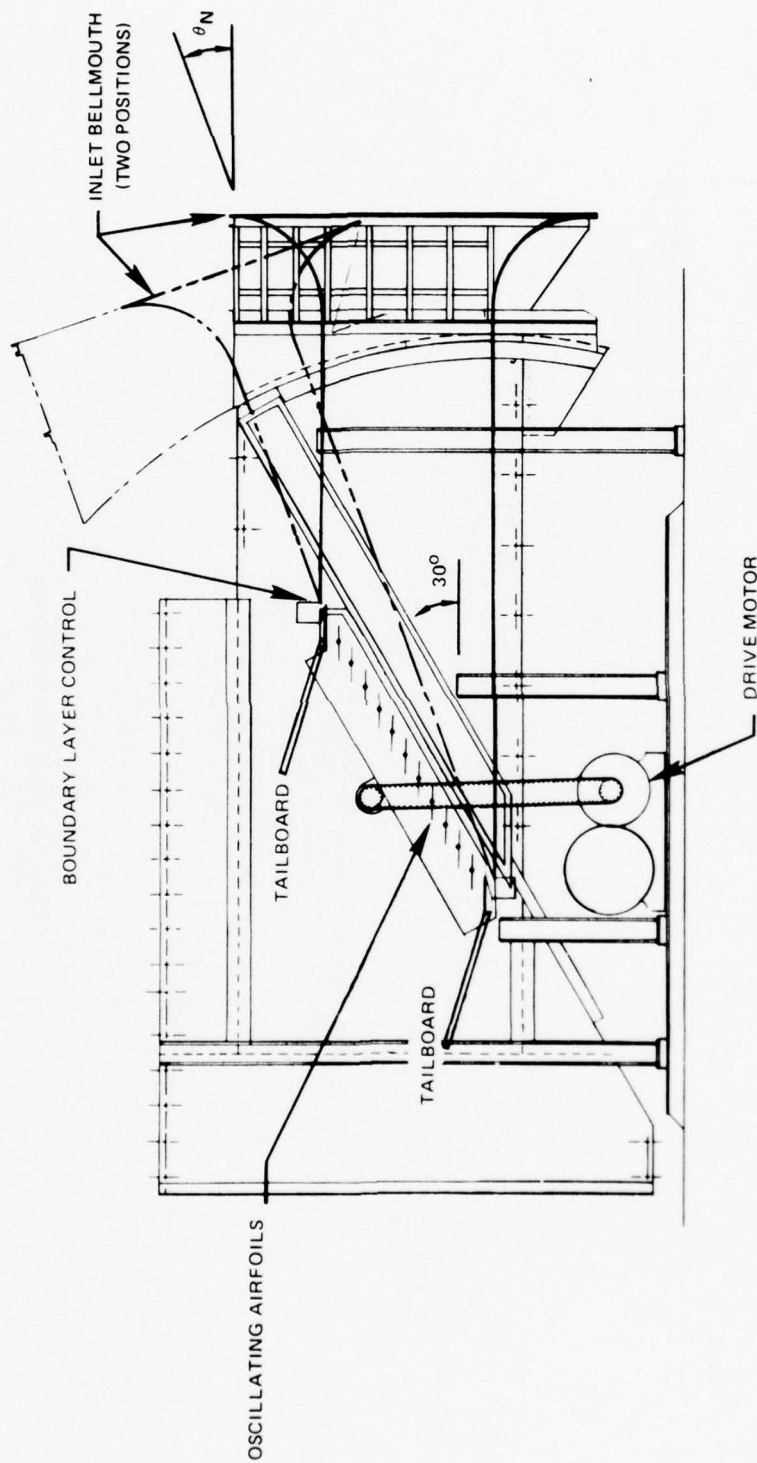


Figure 3 Schematic of Subsonic Oscillating Cascade Wind Tunnel

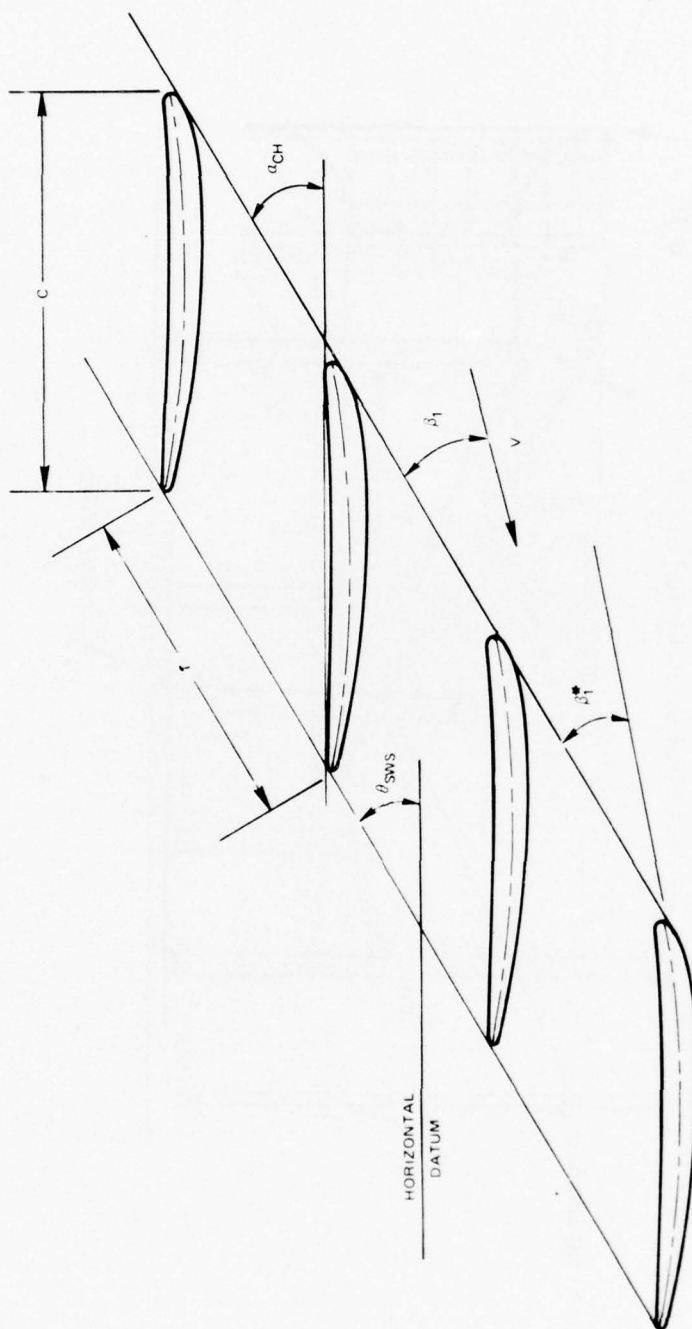
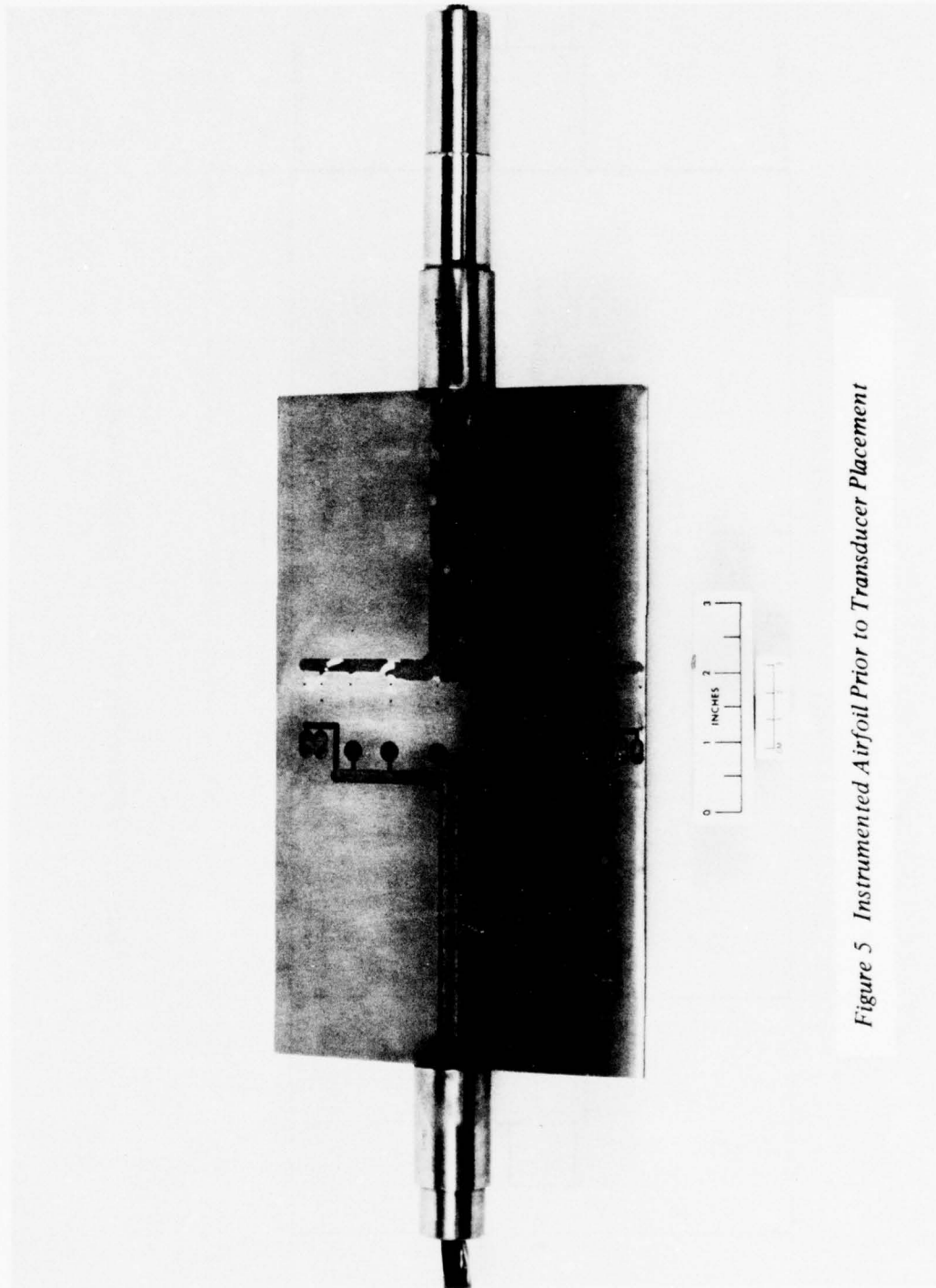


Figure 4 Blade Nomenclature





*Figure 5 Instrumented Airfoil Prior to Transducer Placement*

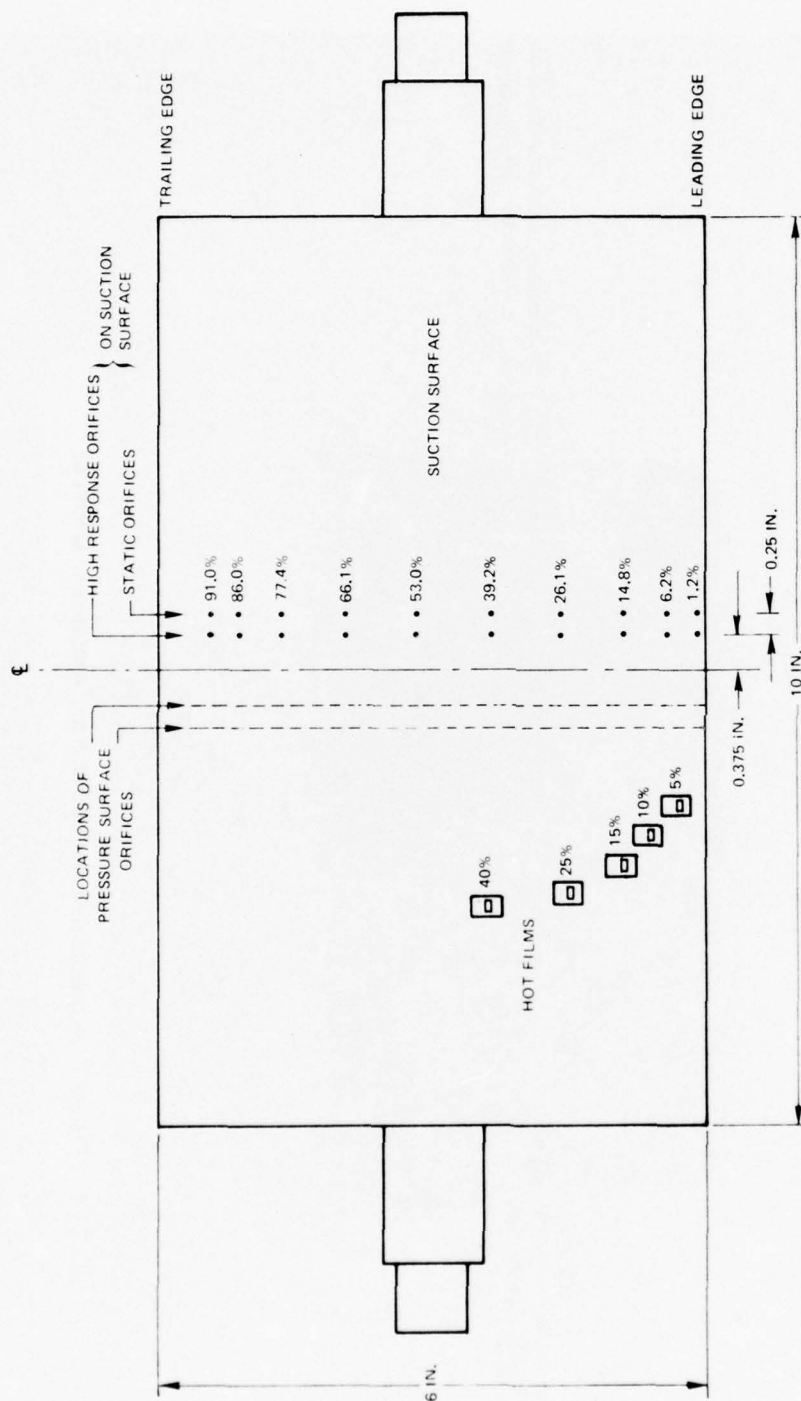


Figure 6 Schematic Plan View of Instrumented Airfoil

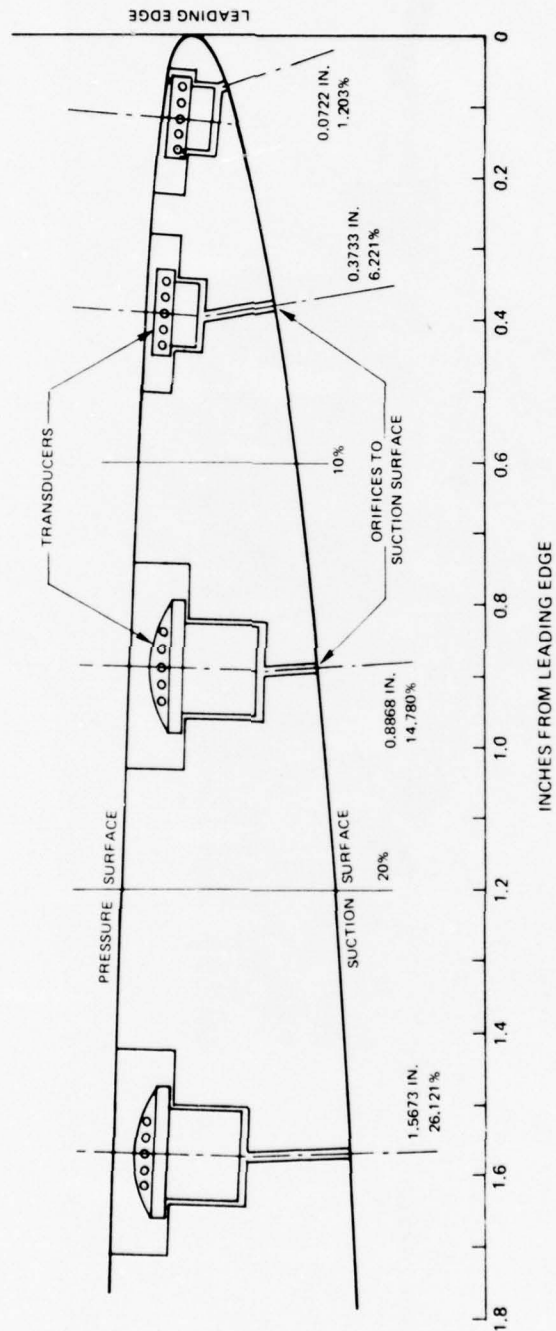


Figure 7 Section View Showing Suction Surface Instrumentation



*Figure 8 Instrumented Airfoil*



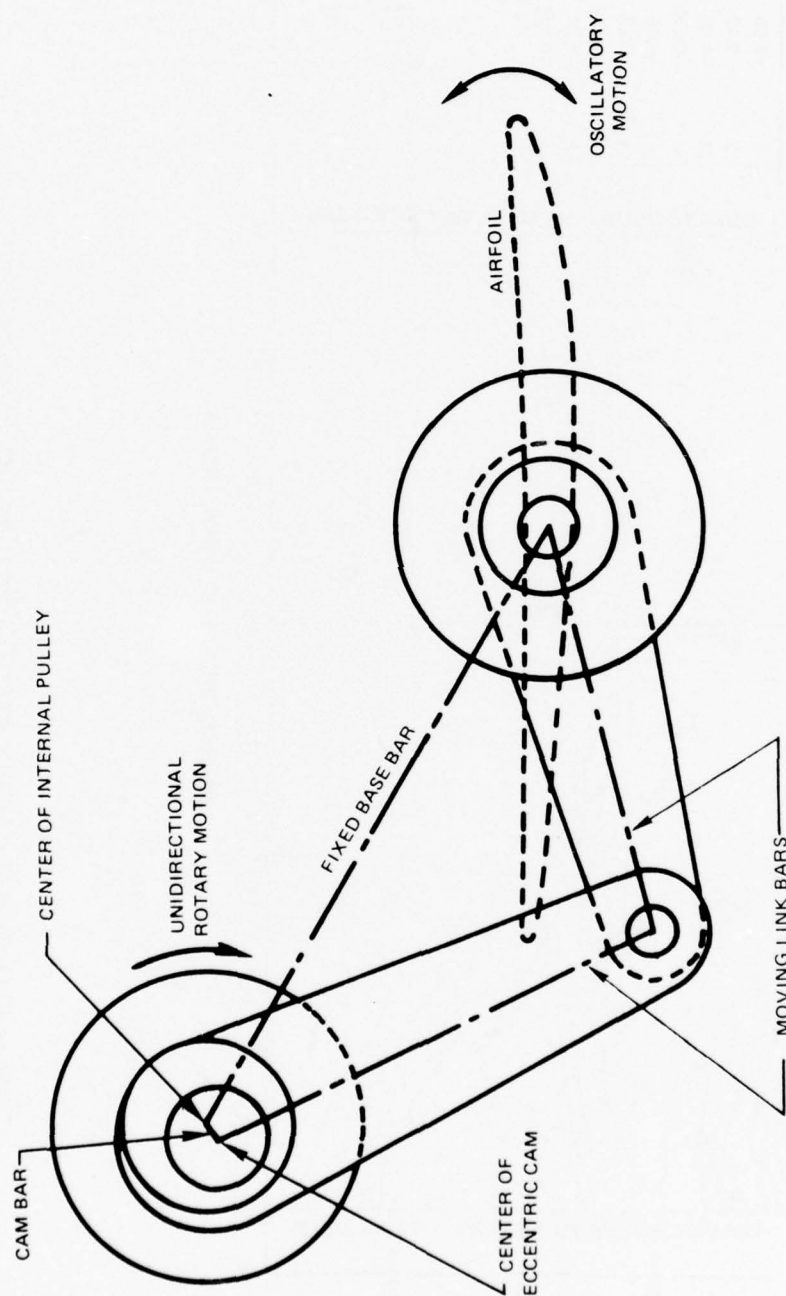


Figure 9 Four-Bar Linkage to Produce Sinusoidal Motion

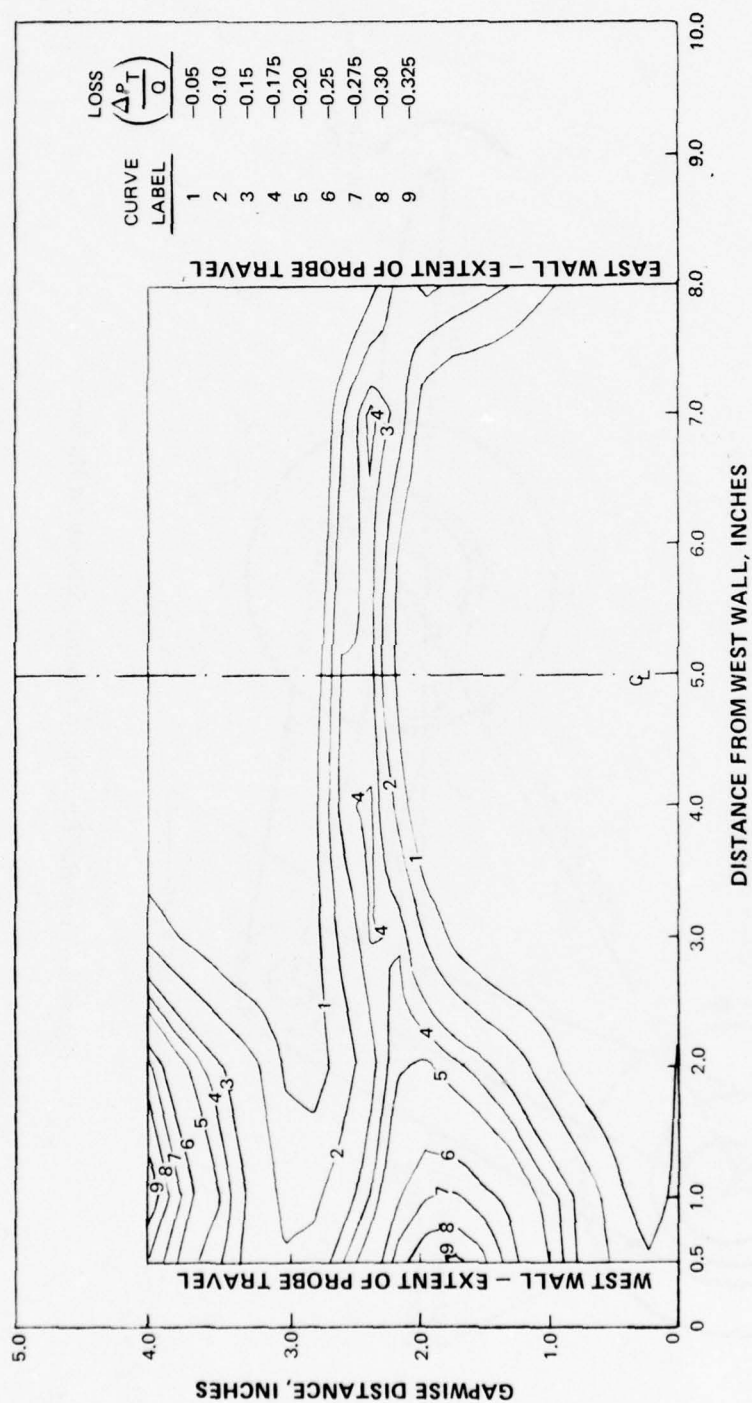


Figure 10 Contour Plot of Wake Rake Traverse (Corrected Flow Condition)

PRATT & WHITNEY AIRCRAFT GROUP

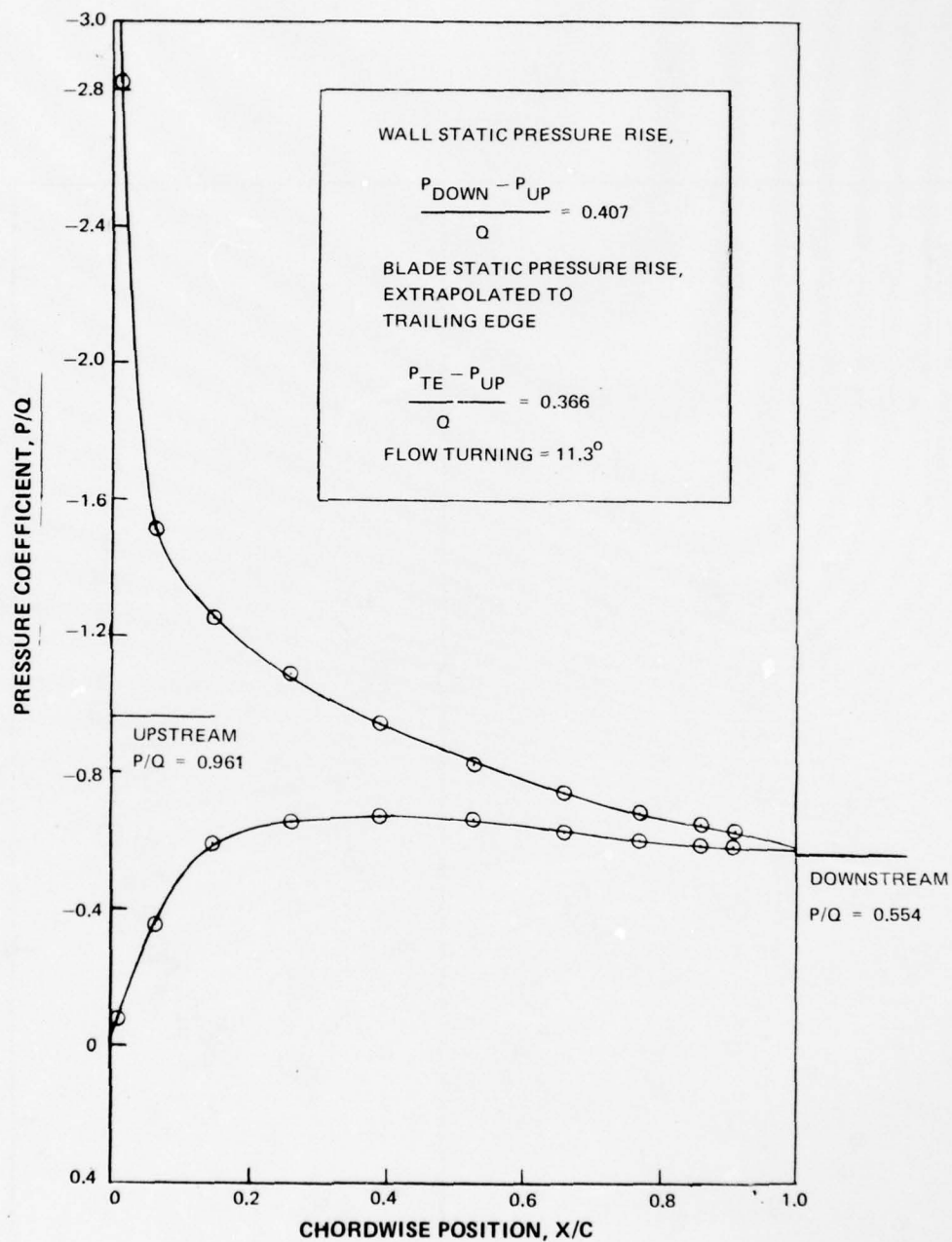


Figure 11 Chordwise Pressure Distribution ( $V_{REF} = 196.51$  f.p.s.)

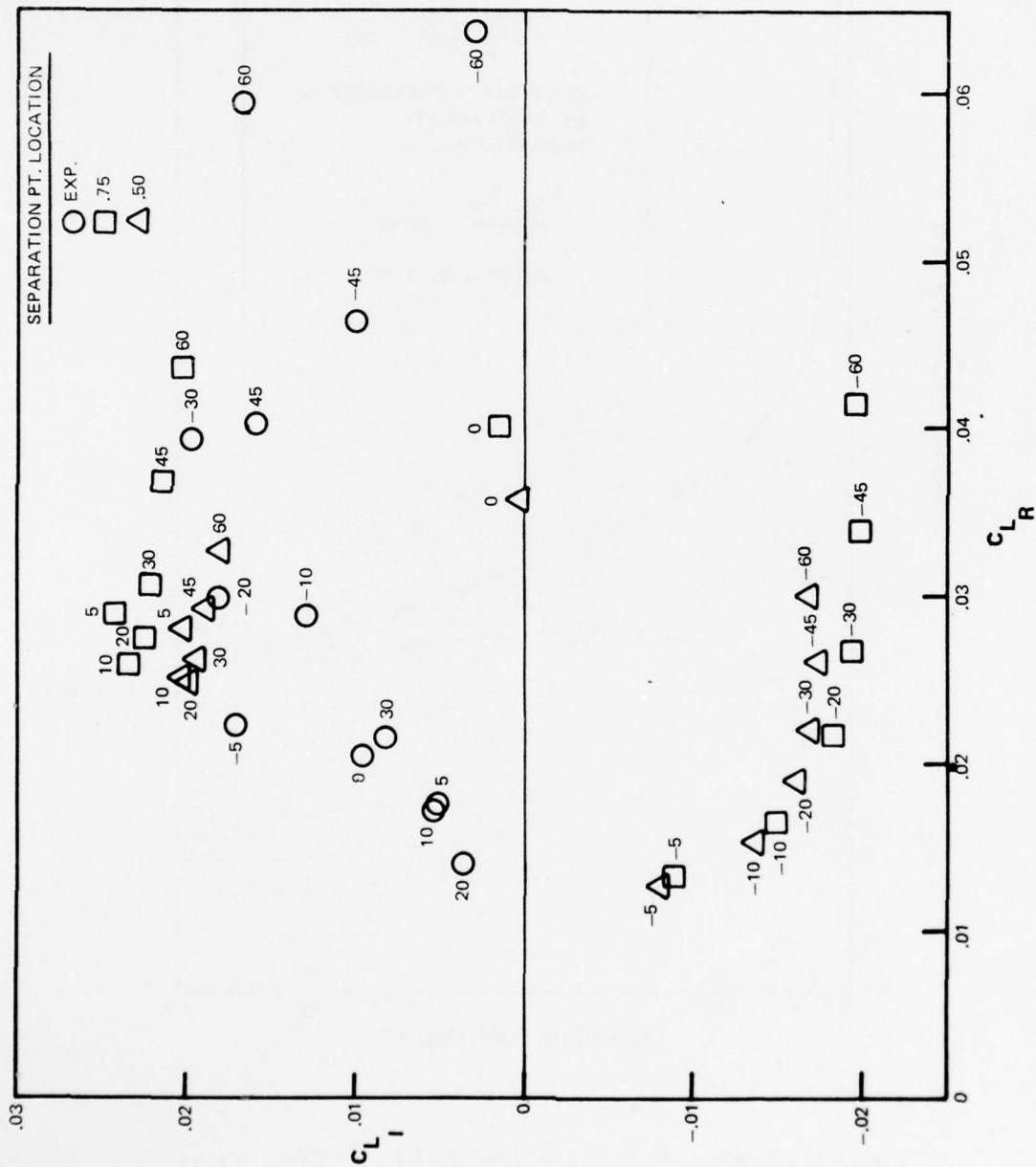


Figure 12 Parametric Variation of Lift Coefficient with Interblade Phase Angle ( $k = .035$ )



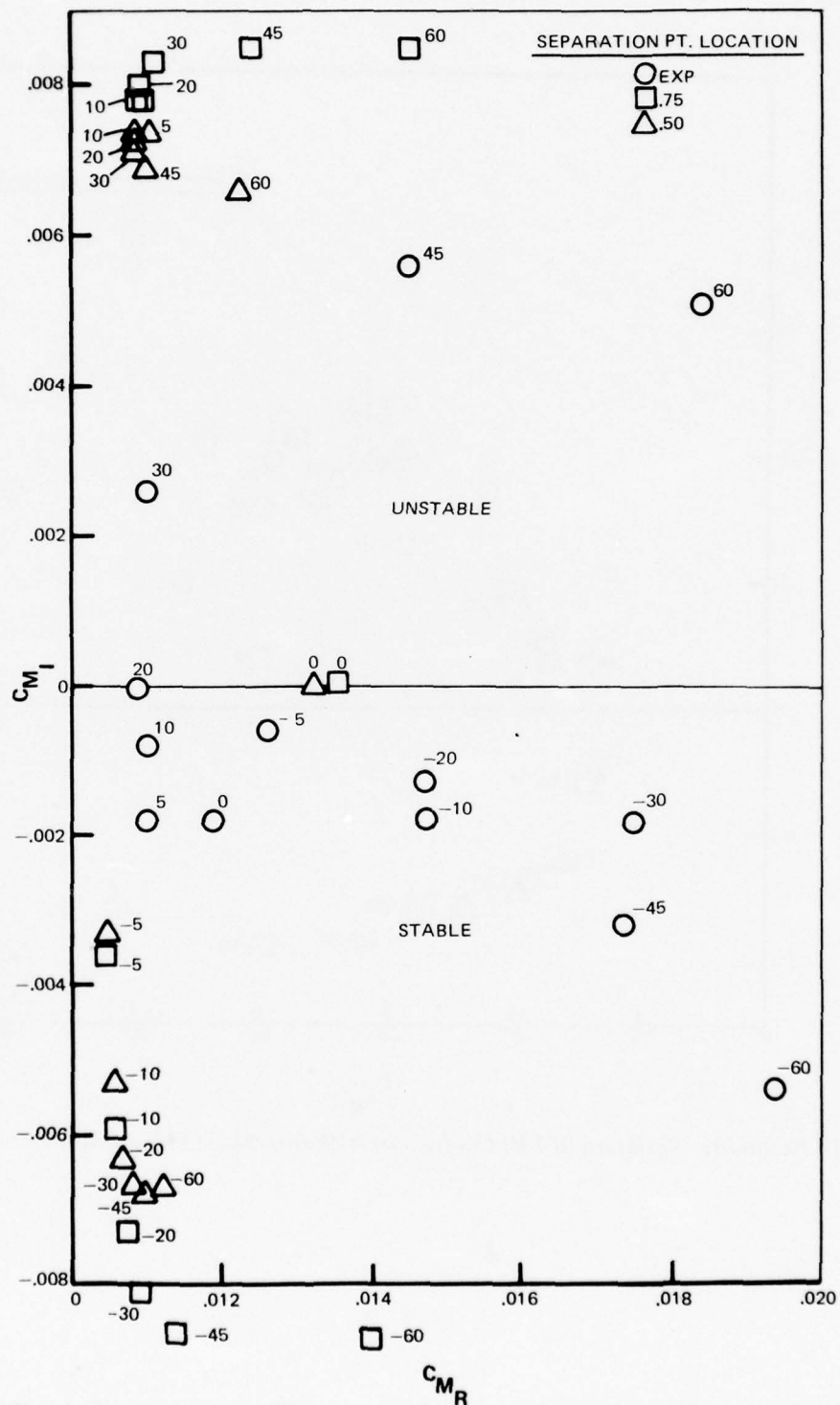


Figure 13 Parametric Variation of Moment Coefficient with Interblade Phase Angle ( $k = .035$ )

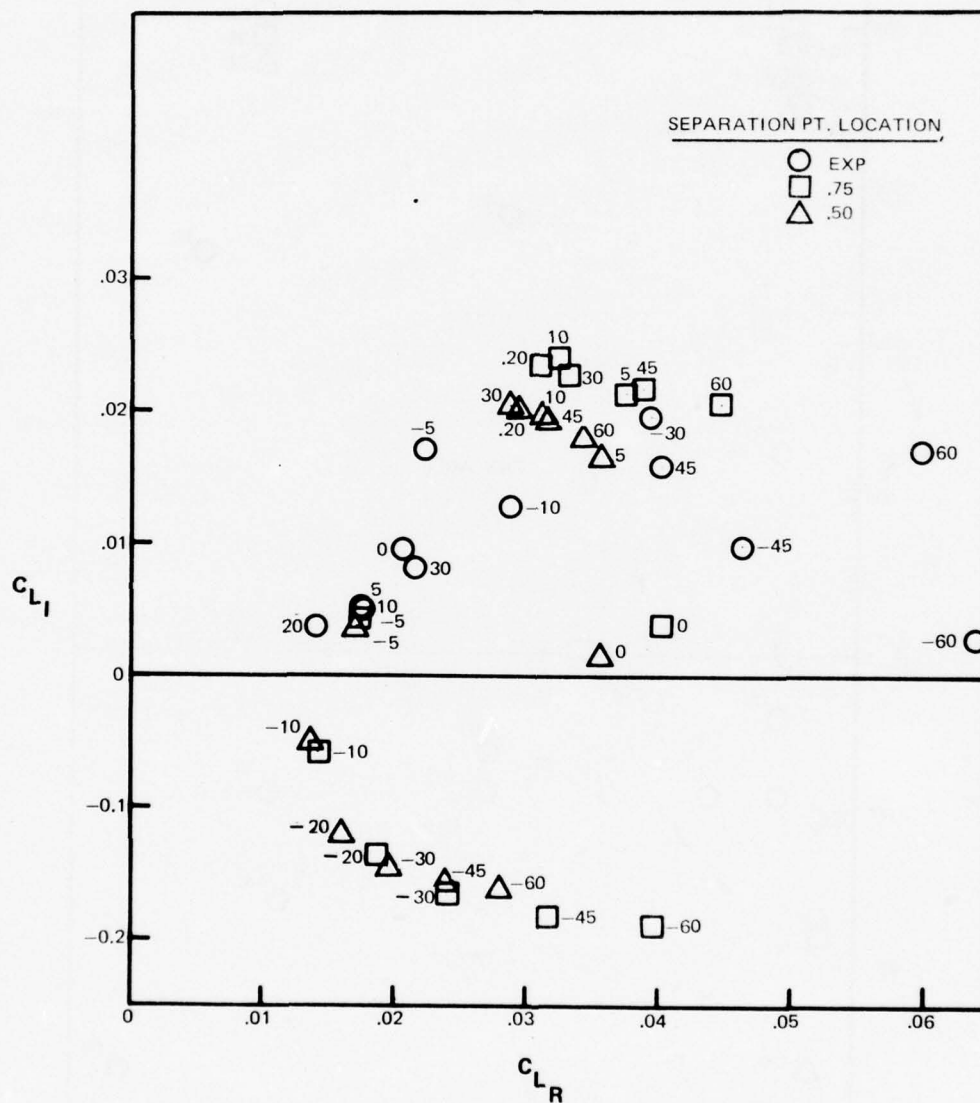


Figure 14 Parametric Variation of Lift Coefficient with Interblade Phase Angle ( $k = .086$ )

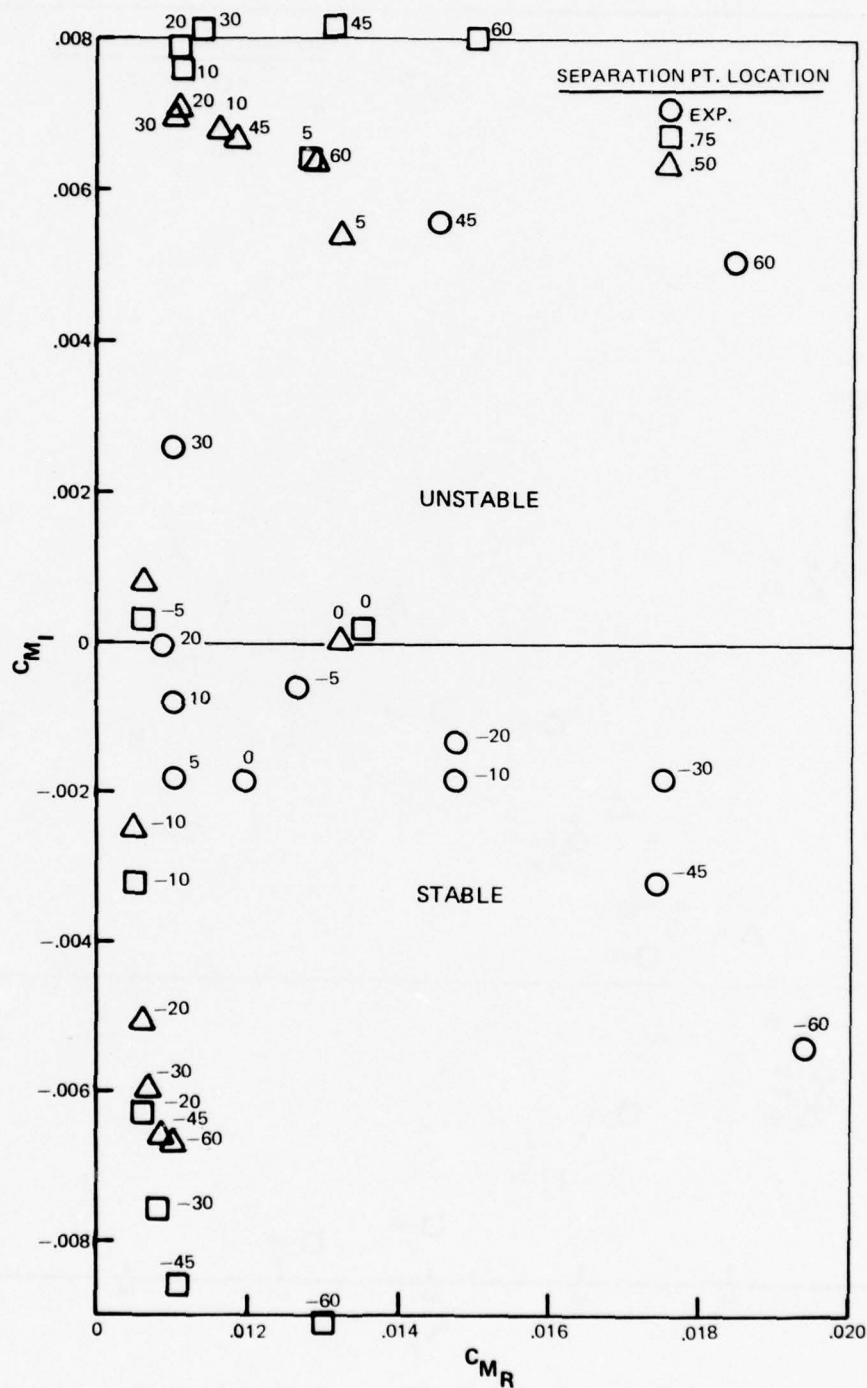


Figure 15 Parametric Variation of Moment Coefficient with Interblade Phase Angle ( $k = .086$ )

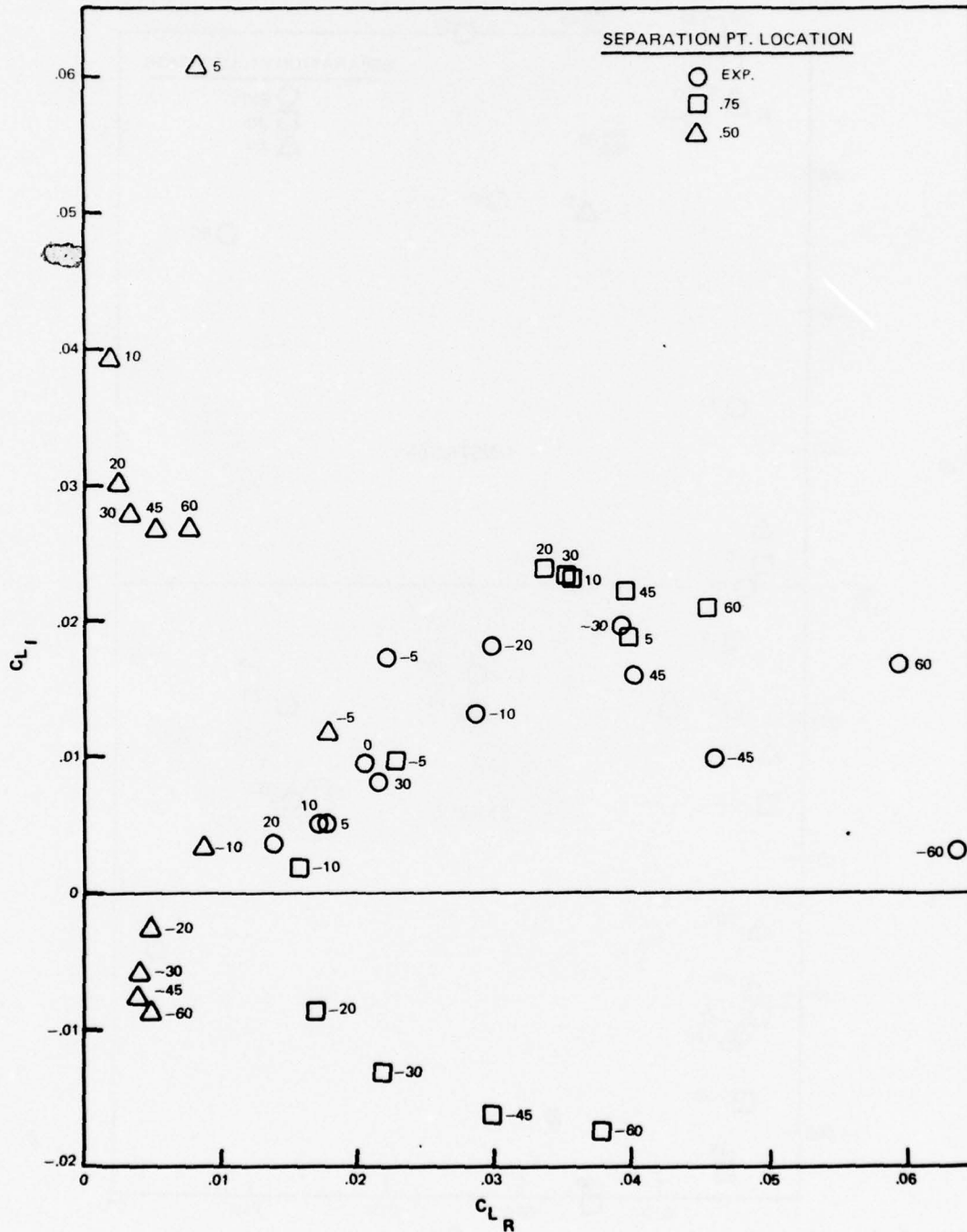
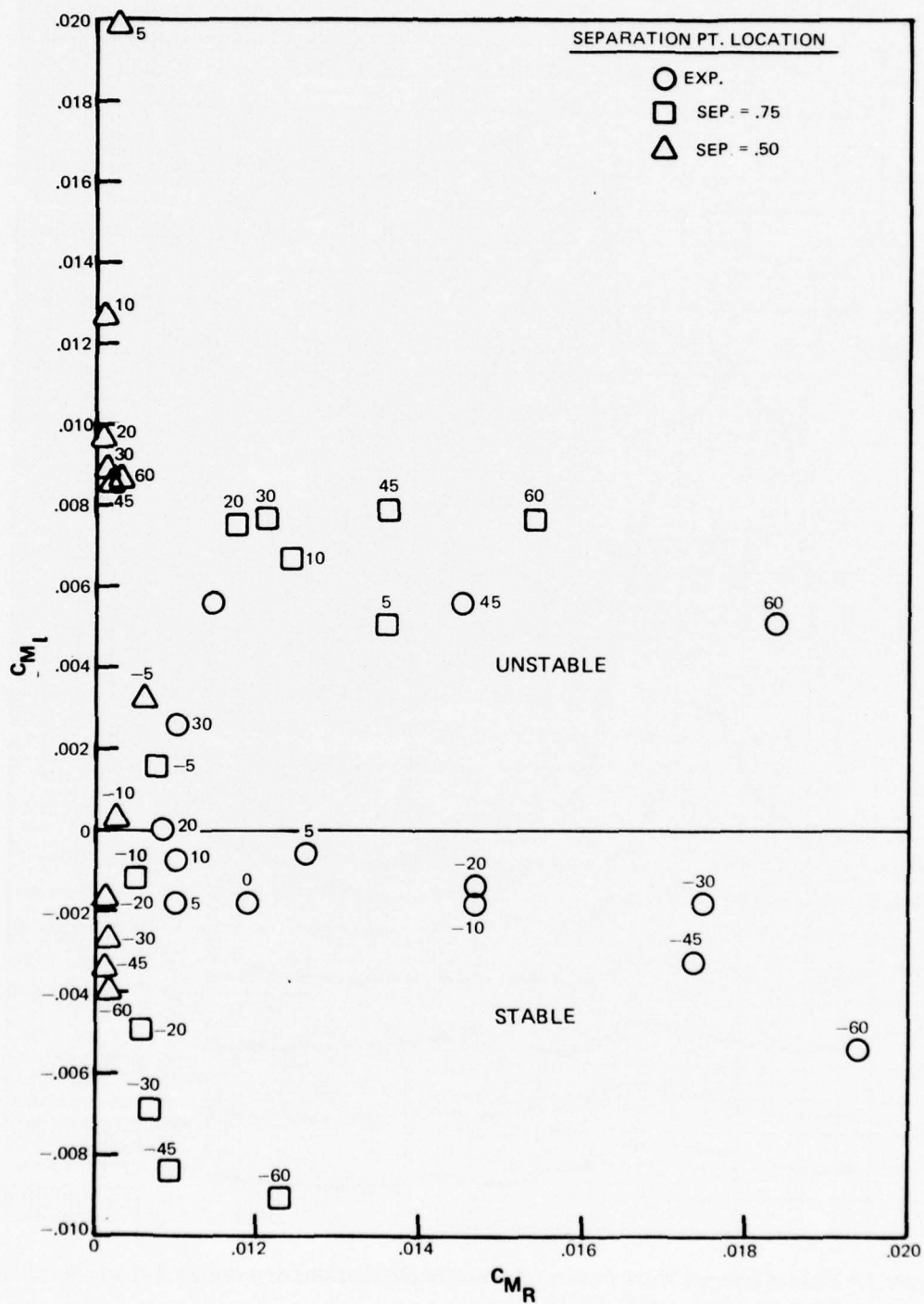


Figure 16 Parametric Variation of Lift Coefficient with Interblade Phase Angle ( $k = .135$ )





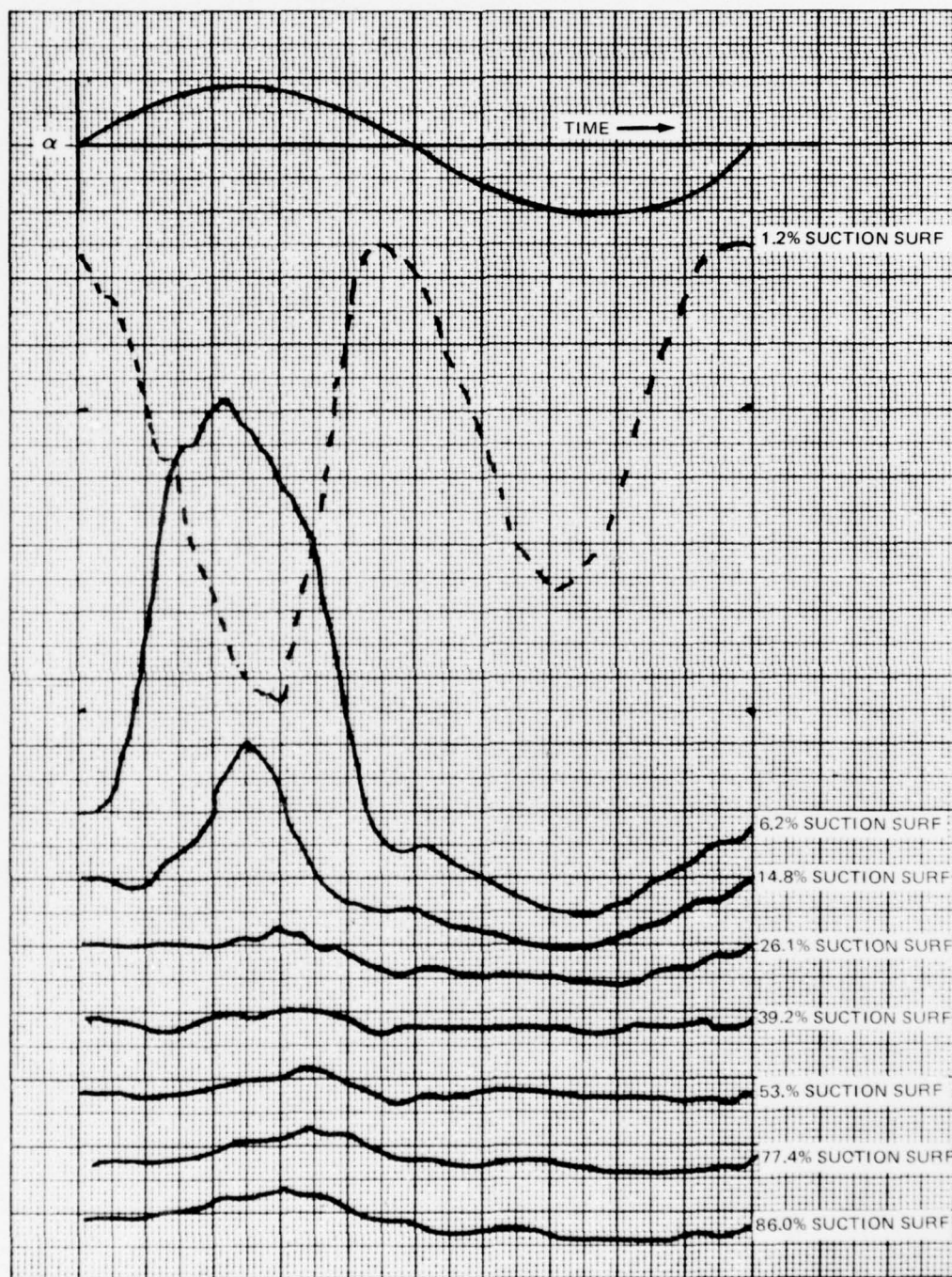


Figure 18 Time-Averaged Wave Forms of Pressure Oscillations at Various Airfoil Chordwise Locations ( $\alpha = +60^\circ$ ,  $f = 17.1$  c.p.s.)

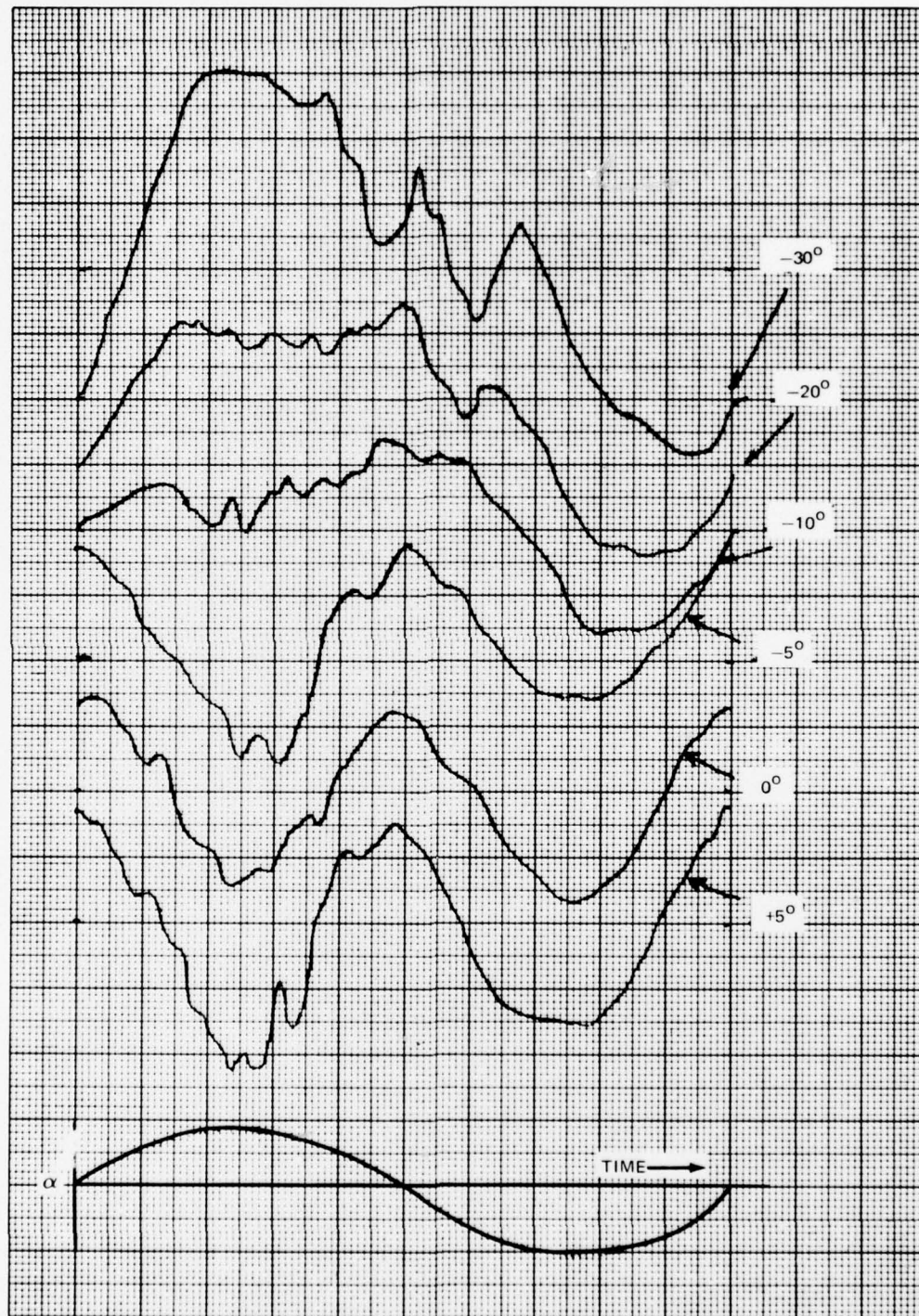


Figure 19 Time-Averaged Wave Forms of Pressure Oscillations for Various Interblade Phase Angles (Airfoil Suction Surface Sensor at 1.2% Chordwise Location,  $f = 17.1$  c.p.s.)



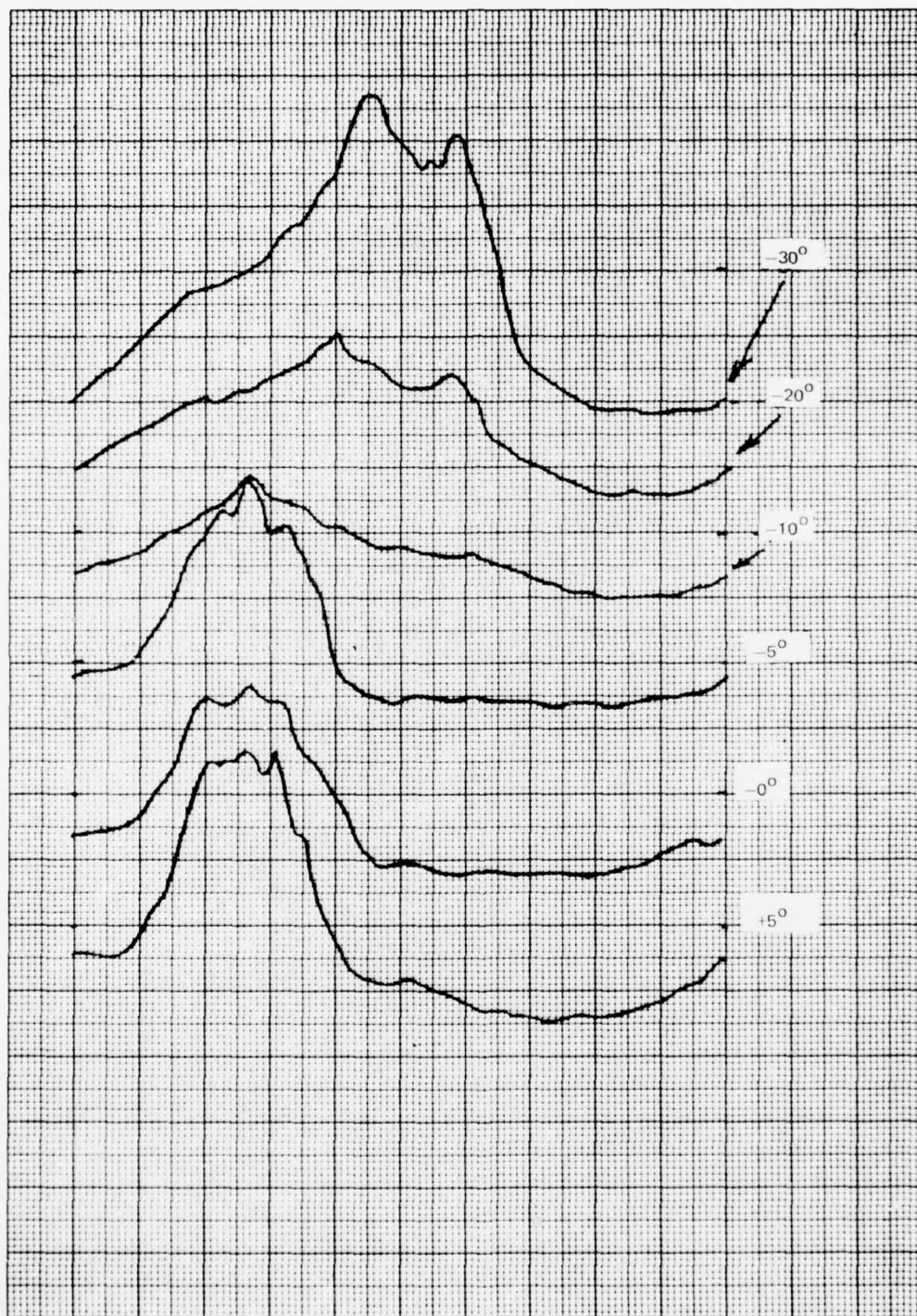


Figure 20 Time-Averaged Wave Forms of Pressure Oscillations for Various Interblade Phase Angles (Suction Surface Sensor at 6.2% Chordwise Location,  $f = 17.1$  c.p.s.)



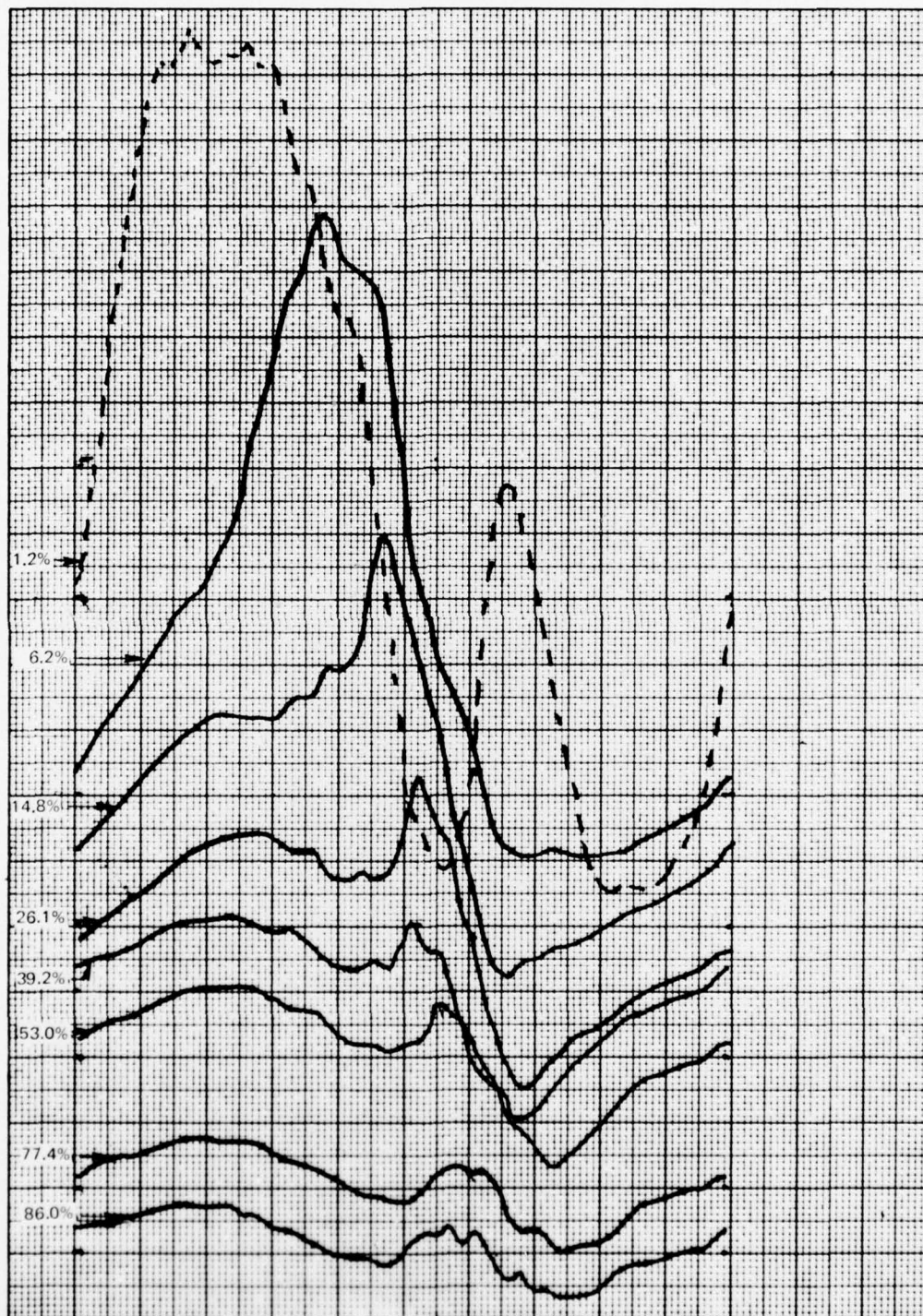


Figure 21 Variation of Unsteady Pressure over Airfoil Suction Surface During One Cycle  
( $\alpha = -60^\circ$ ,  $f = 17.1$  c.p.s.)

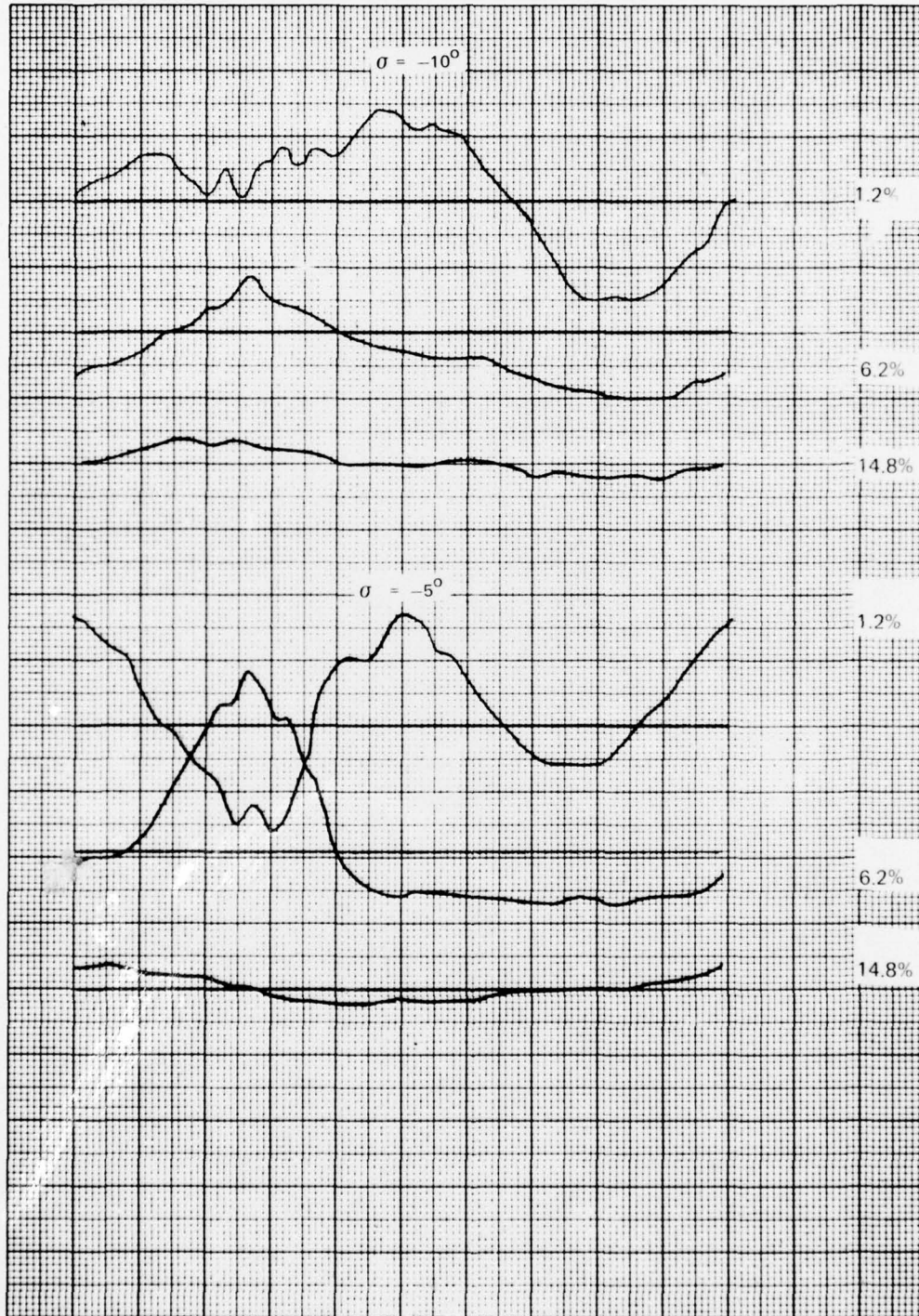


Figure 22 Pressure Response of Three L. E. Suction Surface Sensors at Two Interblade Phase Angles ( $f = 17.1$  c.p.s.)



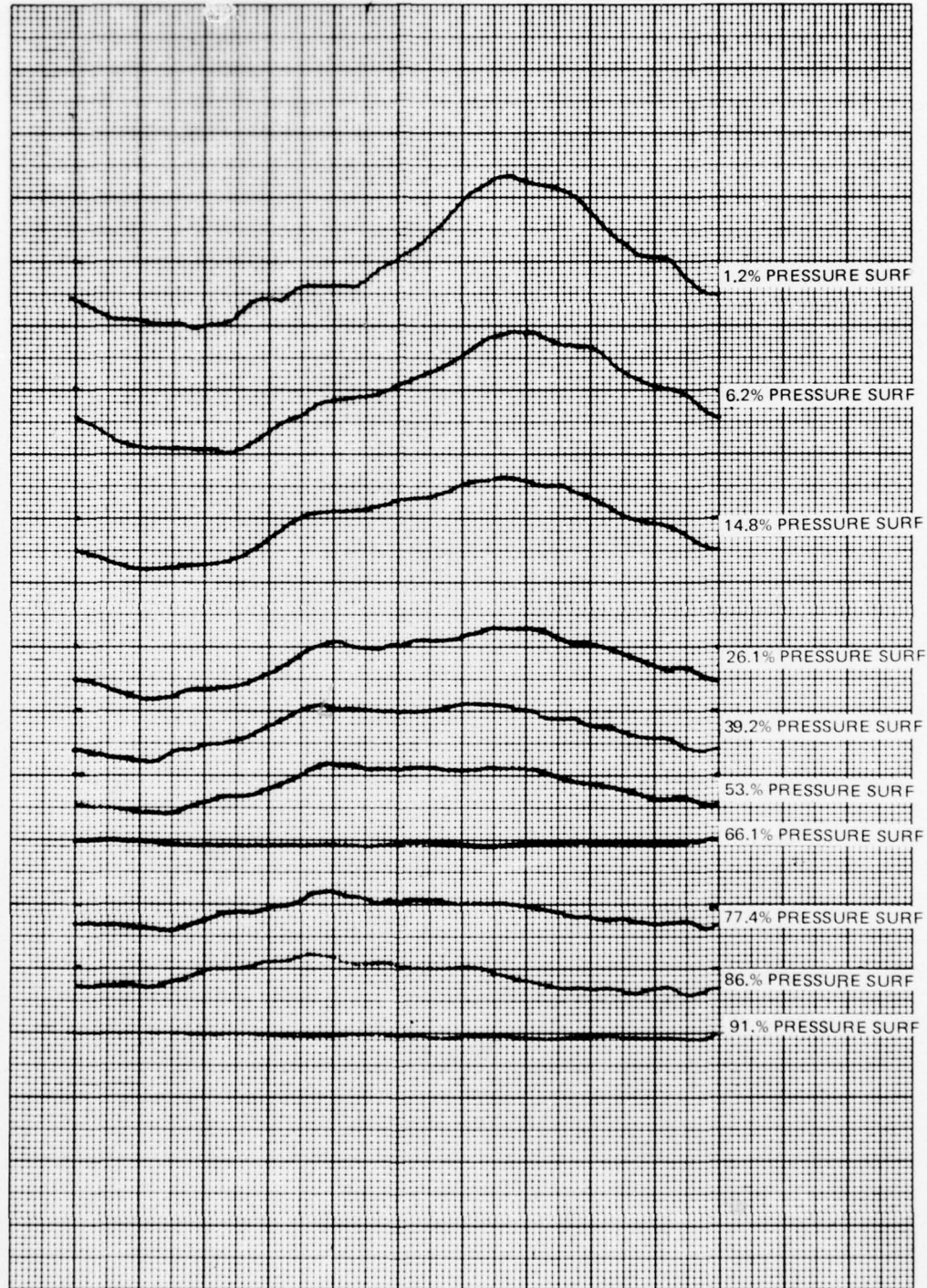


Figure 23 Time-Averaged Wave Forms on Pressure Surface ( $f = 17.1$  c.p.s.,  $\sigma = +60^\circ$ )

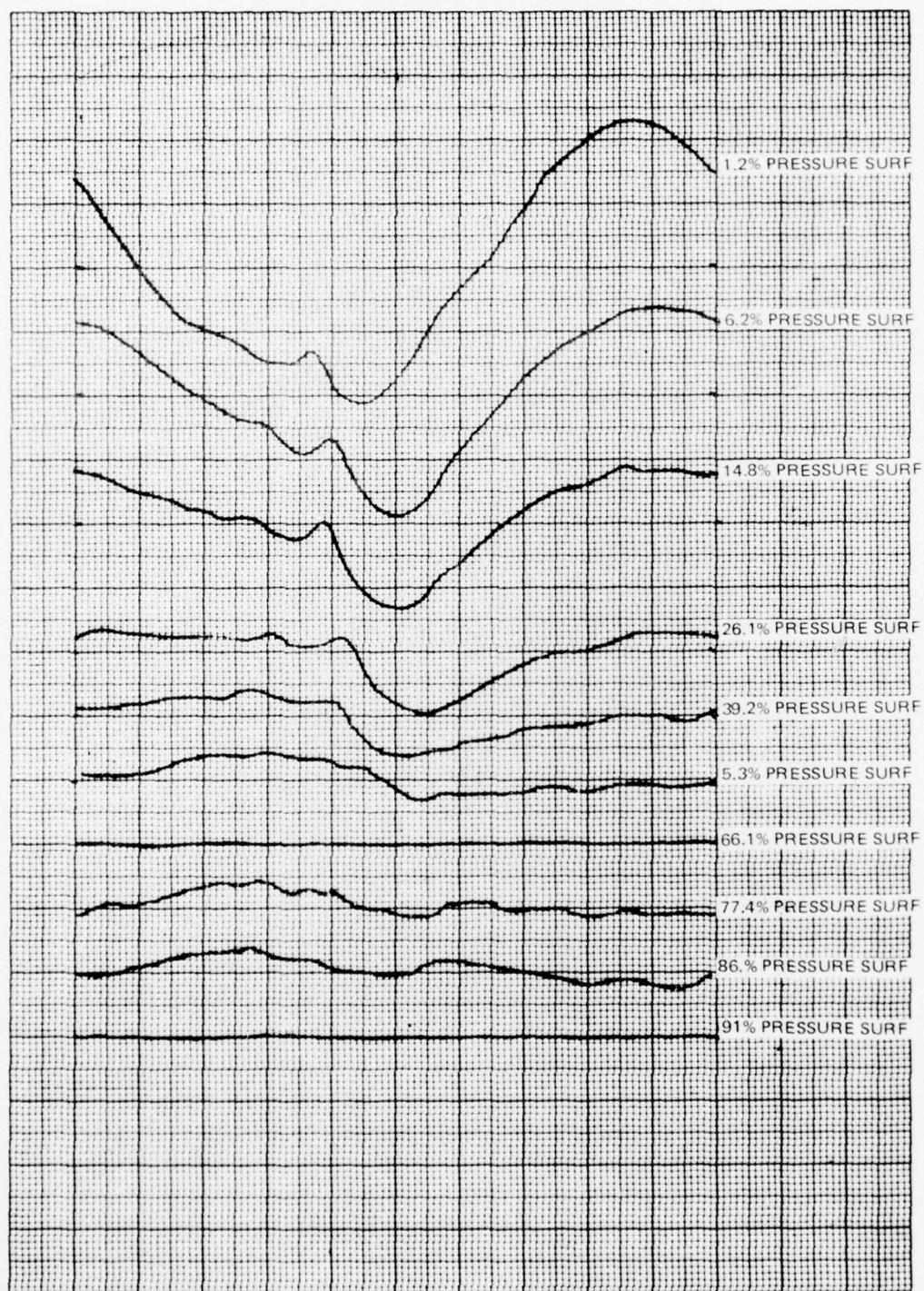


Figure 24 Time-Averaged Wave Forms on Pressure Surface ( $f = 17.1$  c.p.s.,  $\sigma = -60^\circ$ )



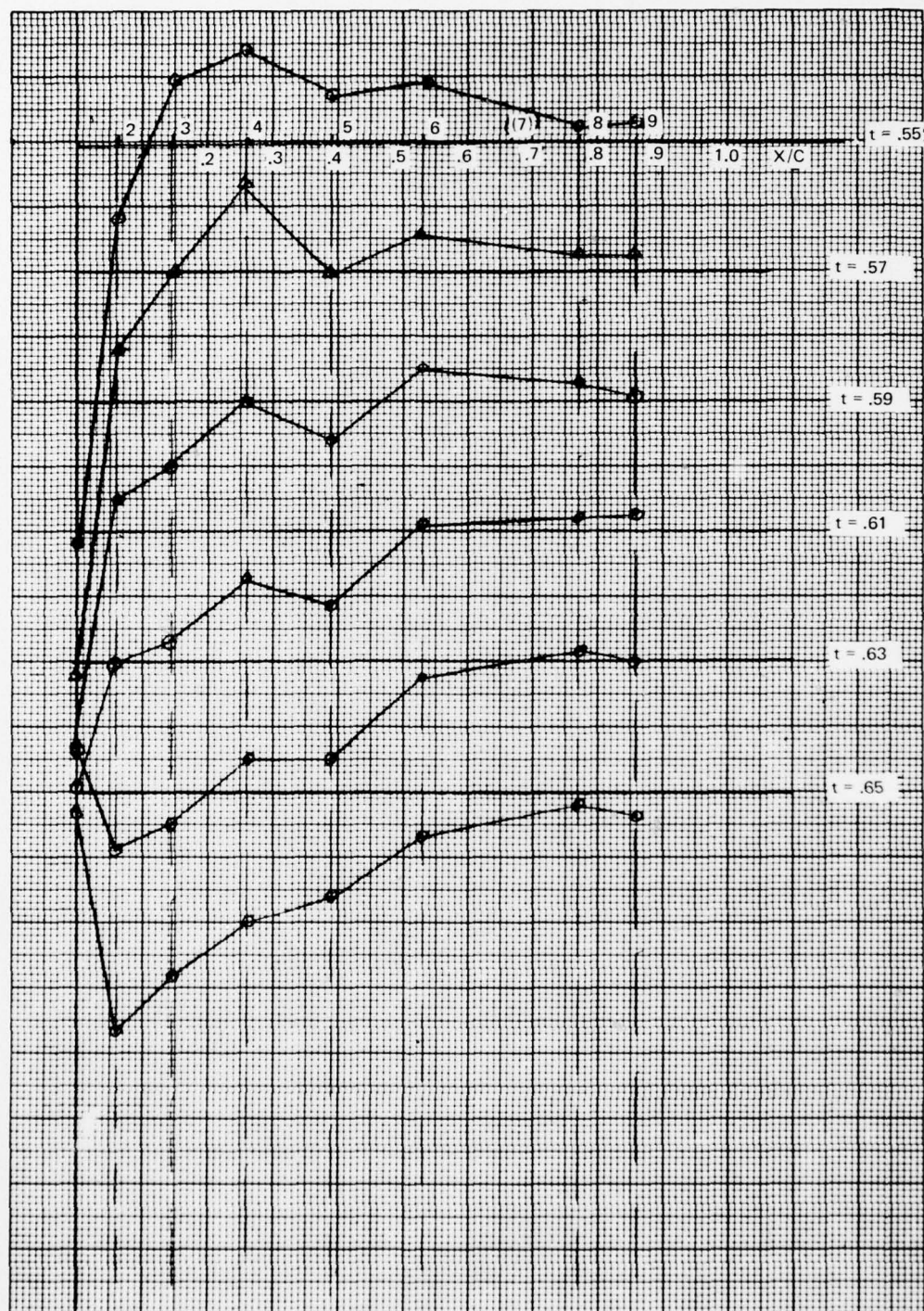


Figure 25 Instantaneous Chordwise Pressure Distribution ( $f = 17.1$  c.p.s.,  $\sigma = -60^\circ$ )



Figure 26 Instantaneous Chordwise Pressure Distribution ( $f = 17.1$  c.p.s.,  $\sigma = +60^\circ$ )

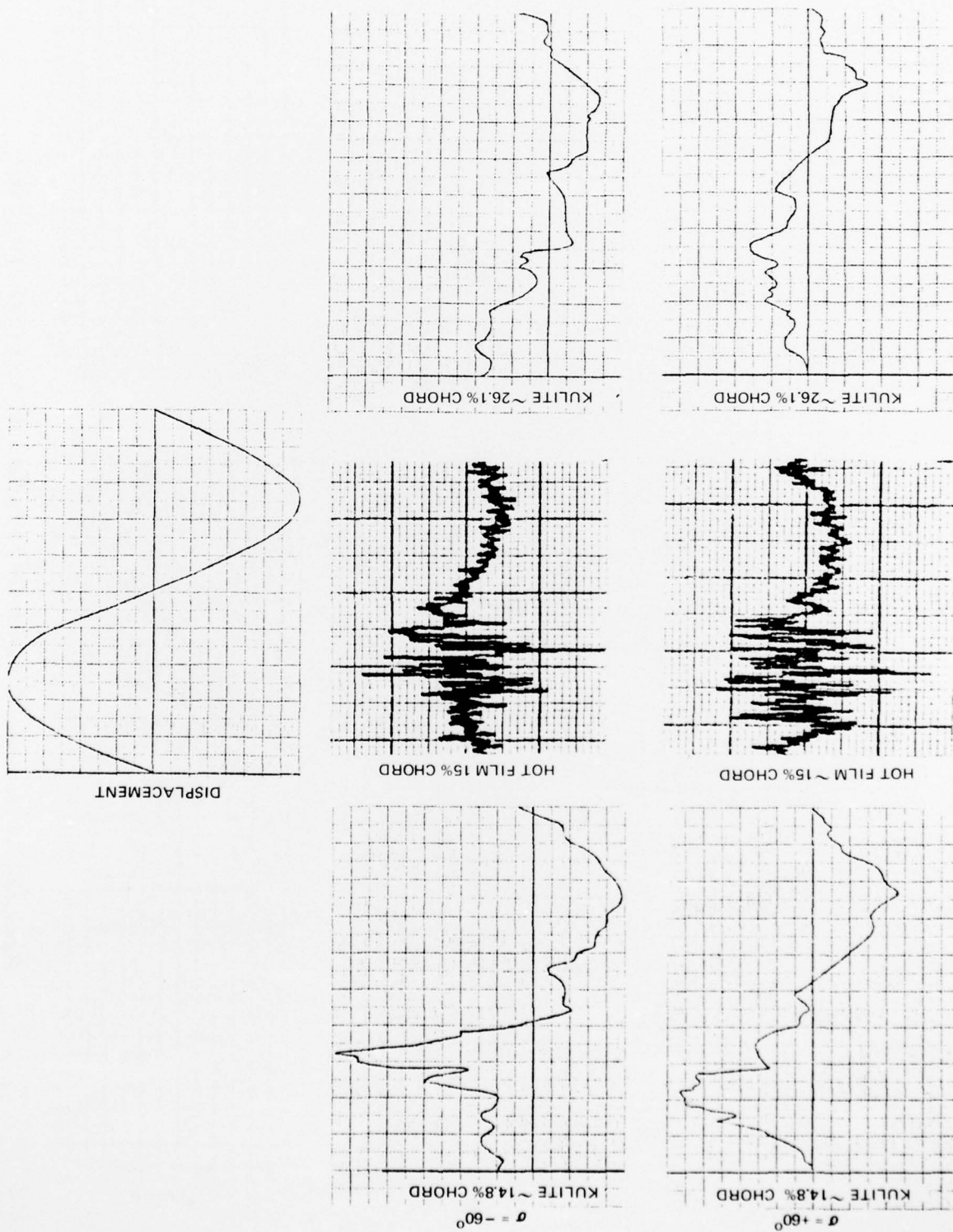


Figure 27 Comparison of Pressure and Hot Film Response for  $\alpha = \pm 60^\circ$  ( $f = 4.5$  cps)



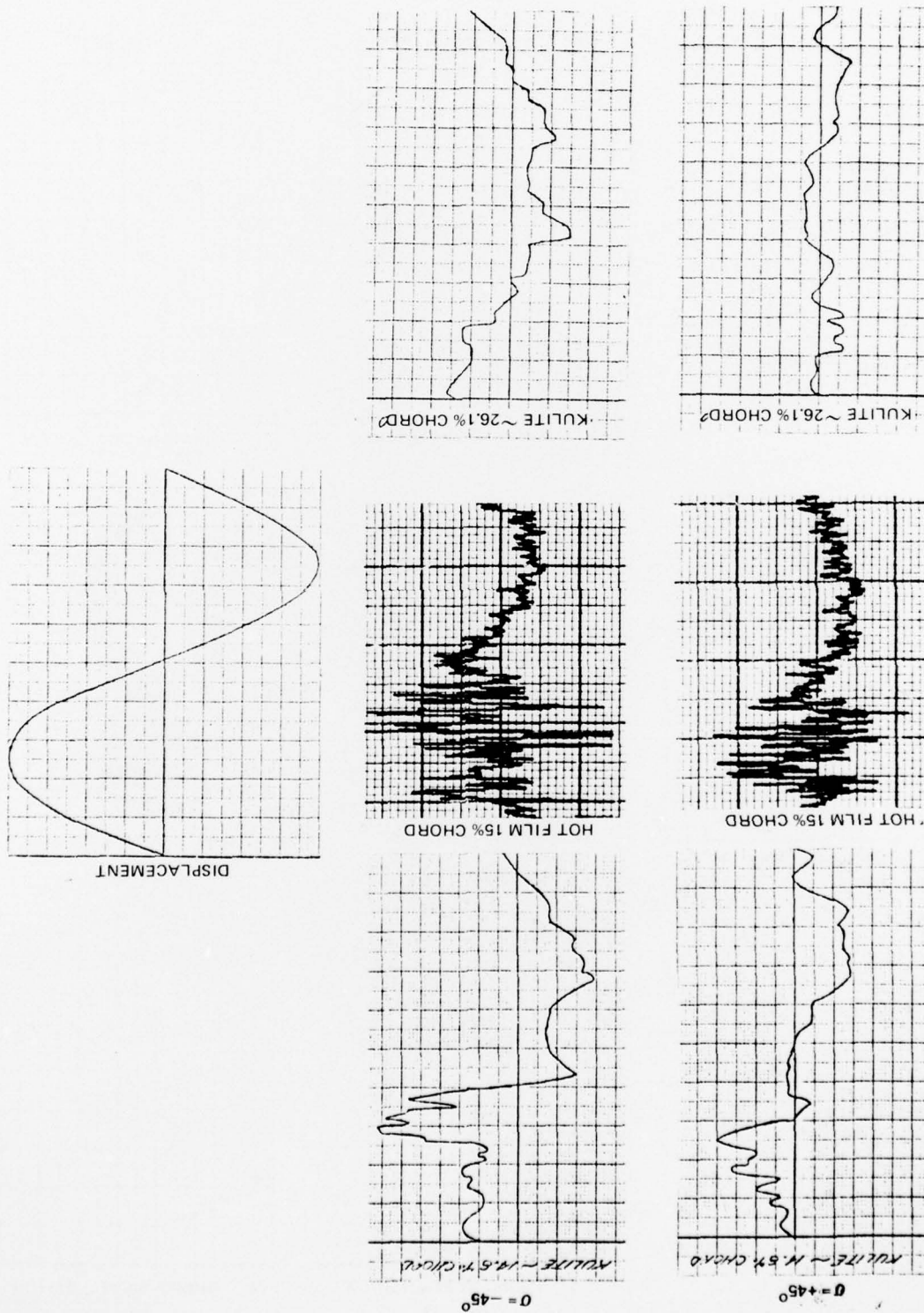


Figure 28 Comparison of Pressure and Hot Film Response for  $\alpha = \pm 45^\circ$  ( $f = 4.5$  cps)



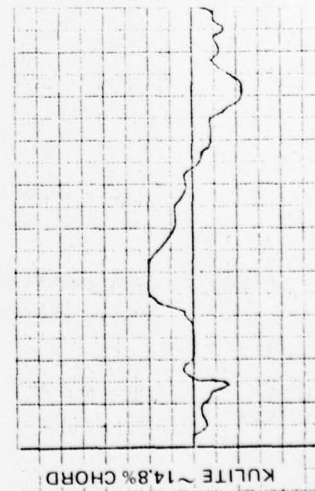
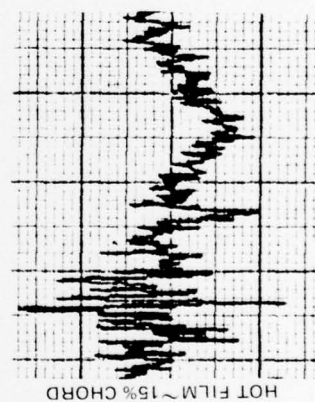
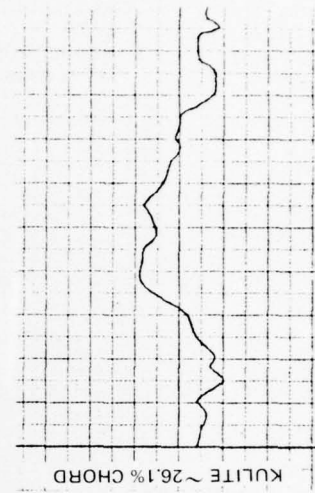
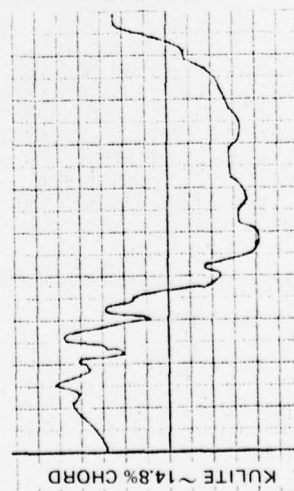
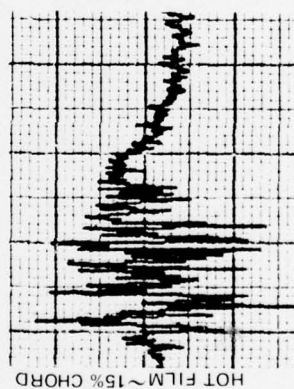
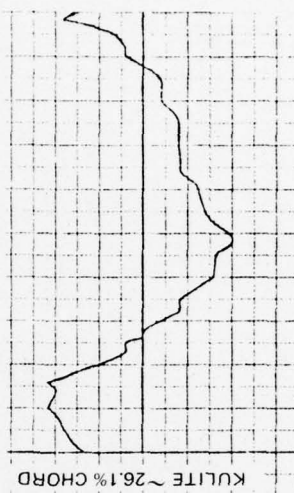
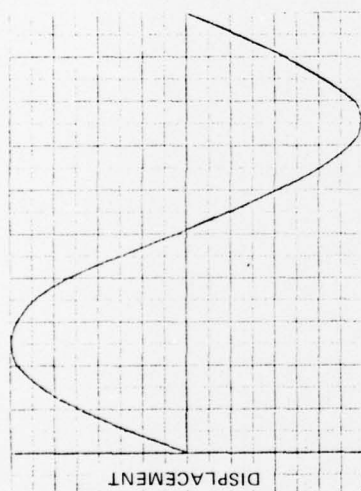


Figure 29 Comparison of Pressure and Hot Film Response for  $\sigma = \pm 30^\circ$  ( $f = 4.5$  cps)

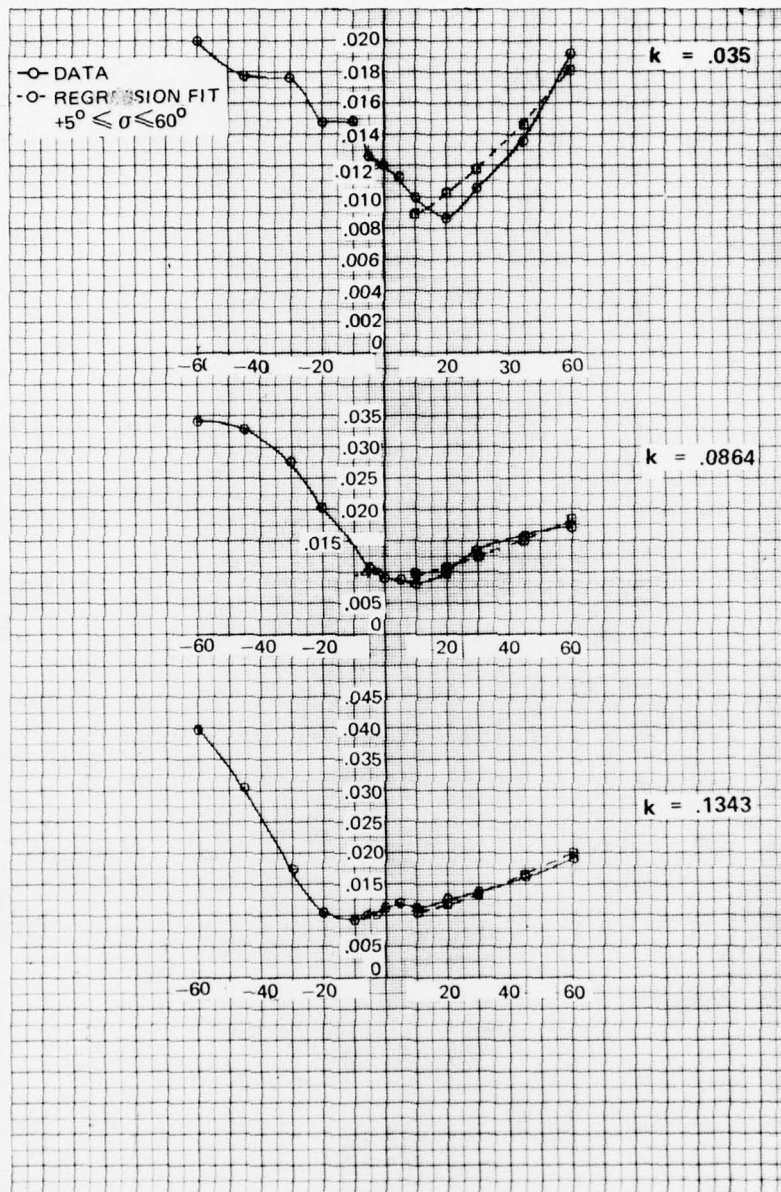


Figure 30 Comparison of Statistical Algorithm and Experimental Data, Moment Coefficient Due to Torsion, Vector Amplitude

PRATT & WHITNEY AIRCRAFT GROUP

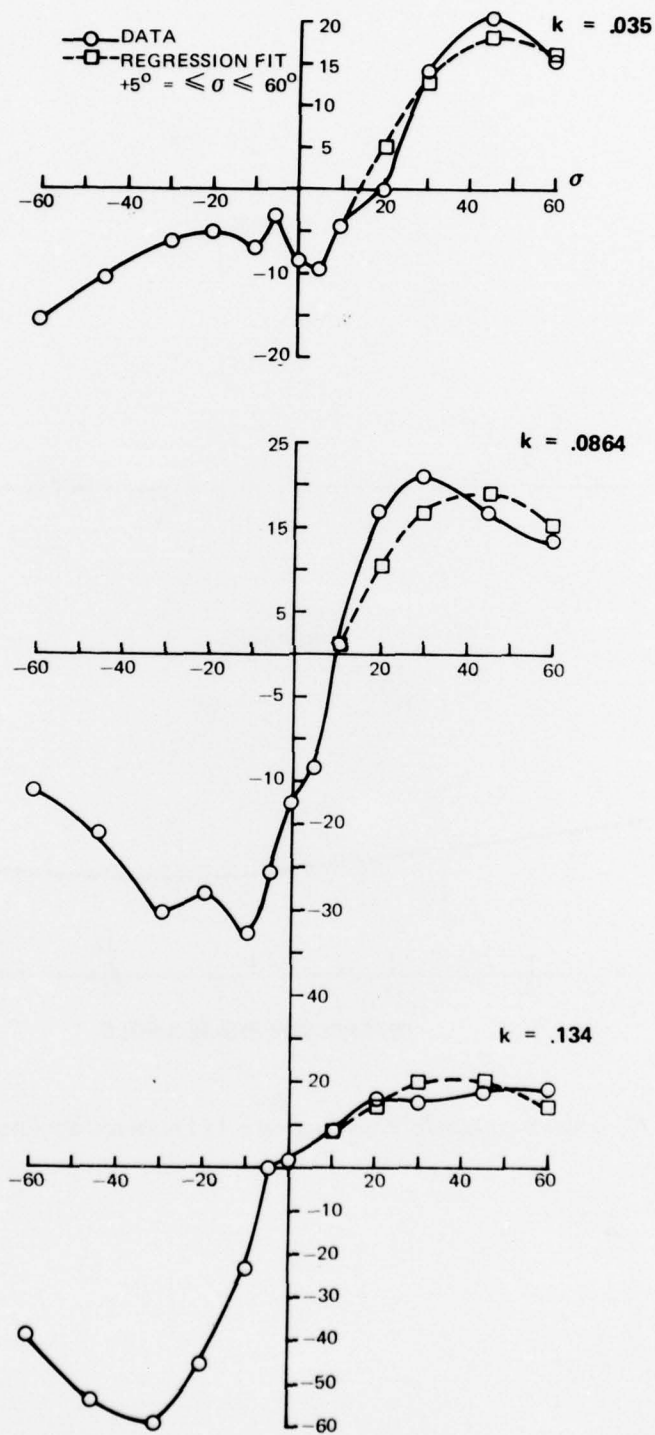


Figure 31 Comparison of Statistical Algorithm and Experimental Data, Moment Coefficient Due to Torsion, Vector Phase Angle

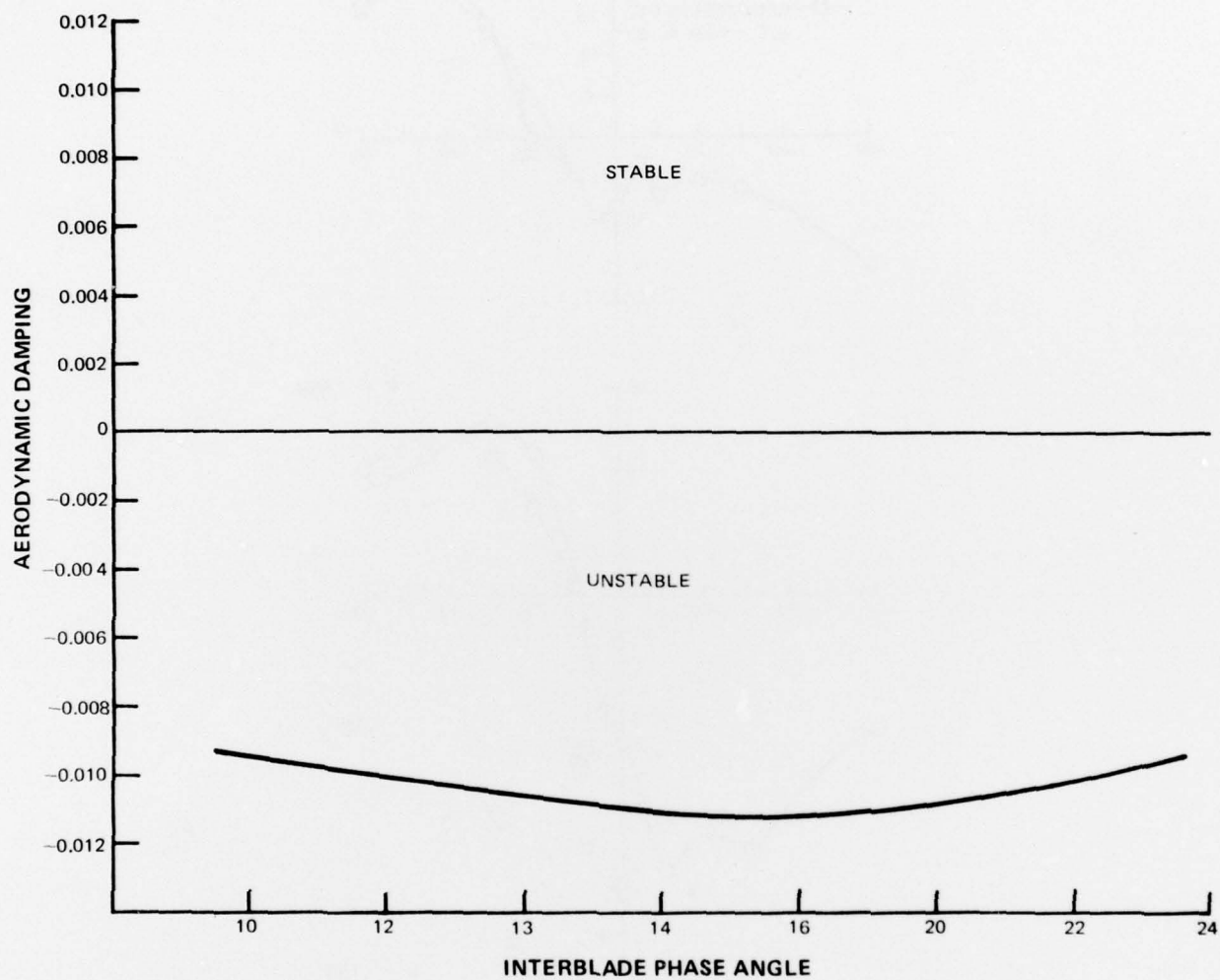


Figure 32 Fan Exit Guide Vane Stability As Predicted By Empirical Algorithm